Deformation reconstruction in a stiffened composite panel using the Inverse FEM method

Candidate: Niccolò Cantele
Student ID:: 306111

Supervisor: Prof. Marco Gherlone
Co-supervisor: Ing. Marco Esposito
Co-supervisor: Ing. Matteo Sorrenti

Academic Year 2023/2024

Polytechnic University of Turin
Master's Degree in Aerospace Engineering

Abstract

The objective of this thesis is the analysis of a wing made of a stiffened composite panel, using the Inverse Finite Element Method (iFEM).

The iFEM method is a structural analysis method that, like the traditional FEM method, involves creating a model that represents the real structure and divides it into elements, in this case, inverse elements.

An iFEM model of the wing has been created using both a hybrid model of shell (2-D) and beam (1-D) elements, as well as a model composed exclusively of 2-D elements.

The iFEM method requires a certain number of experimentally measured strains as input and, based on these, reconstructs nodal displacements and nodal rotations through the minimization of an error functional, which accounts for the difference between measured and calculated strains.

A strain calculation code has been implemented that, based on displacements and nodal rotations obtained from an iFEM analysis software, reconstructs the strains as output across the entire structure.

An experimental test was conducted with a real panel model. Strains were measured at specific points using sensors, such as Fiber Optics, to provide input for the iFEM method and later verify if there was a real correlation with the numerical results.

Moreover, by using the same iFEM models but with fewer measured strains as input, the aim was to verify whether the reconstructed strains in both sensorized and non-sensorized parts of the structure were accurate or not.

Contents

1   Introduction

The objective of this thesis is the analysis of a wing made of a composite stiffened panel using the Inverse Finite Element Method (Inverse FEM or iFEM).

The wing is a real component on which an experimental test was conducted with the final goal of measuring its deformations and displacements at specific points using sensors.

The deformations measured in the test are the input for the iFEM method, which, as will be explained later, reconstructs the nodal degrees of freedom of the model—i.e., displacements and rotations—starting from the geometry of an iFEM model and a certain number of experimentally measured deformations.

To verify the effectiveness of the reconstruction, some of the reconstructed displacements were compared with the corresponding measured displacements.

Subsequently, starting from the degrees of freedom reconstructed using the iFEM method, deformations were calculated both at the points where measurements were taken and in the rest of the panel, through a procedure that is explained below.

The objective in this case is to verify that the iFEM method is accurate in reconstructing the degrees of freedom and that the deformation calculation method is accurate in computing the deformations.

Finally, it was desired to verify whether the iFEM method is able to reconstruct the deformations at the points where they were experimentally measured, in the case where the number of input data to the iFEM code is smaller than in the real case.

For this reason, two types of iFEM models were created: one model with a 'full' sensor configuration, which is faithful to the laboratory configuration, and one model with a 'reduced' sensor configuration, with a smaller number of sensors compared to the experimental setup.

In both the full case and the reduced case, two iFEM models were created: one entirely made up of 2-D elements and one hybrid model, consisting of both 2-D and 1-D elements.

1.1   Methods for reconstructing displacements from the measured deformations

The Inverse FEM method is a shape-sensing technique that allows the reconstruction of the degrees of freedom of a structure from deformations experimentally measured by sensors.

This method has been studied and refined in many works, especially for structures modeled with iFEM 1-D (beam) and 2-D (shell) elements.

To reconstruct the displacements, the first option is the numerical integration of the experimentally measured deformations. In this case, a large number of measurements is required.

The second option for reconstructing displacements and rotations is the linear combination of basis functions. In this case, it is necessary to define the basis functions, for example by choosing the vibrational modes of the structure, and the weights, which could, for instance, be derived from the measured deformations.

Furthermore, there is the possibility of applying Neural Networks[33].

Finally, there is the shape sensing method based on the variational principle, which will be explained later.

1.2   Shape Sensing Methods

Two well-known examples of shape sensing methods are the Modal Method (MM) and iFEM. The Modal Method is based on expressing deformations and displacements as modal shapes and modal coordinates [23],[24]. The modal coordinates are calculated by fitting the deformation field to the measured deformations. In [23], for example, the modal coordinates and shapes were experimentally measured to predict the static deformation of an aluminum cantilever plate. A key factor in this case was also the number and positioning of the sensors.

In literature, there are comparative studies that use both the MM and the iFEM. In [25], for example, the case of a wing-shaped plate was analyzed, and it was highlighted that the iFEM is more accurate. However, this statement is not generally valid, as demonstrated by studies [26] and [11], conducted on a numerical model of a wing box, where it was found that the MM can be more accurate than the iFEM when there is a limited number of sensors.

Another shape sensing method, developed by Shkarayev et al. [27], involves reconstructing the aerodynamic load applied to a structure from the measured deformations. The load is expressed as a combination of known distributions that cause deformations, which are compared with the measured ones to determine the weight of each distribution in contributing to the load.

If an additional step is added to the load reconstruction, namely the calculation of displacements through the analysis of a FEM model of the structure, the method is called the "2-steps method" [28], [29]. This method, which has proven accurate in the numerical analysis of aerospace components, allows for the calculation of both the load and the displacements of a structure.

In [22], the results of the structural analysis of an aluminum stiffened panel (a typical aerospace component) are compared, using three different shape sensing methods: the MM, the iFEM, and the 2-steps method. This study demonstrates that the iFEM method is superior to the others in terms of accuracy, but it also shows that both the MM and the 2-steps method are effective in reconstructing the deformation of the stiffened panel.

Furthermore, this study highlighted how the MM is highly influenced by the choice of modal shapes and coordinates, while the 2-steps method requires a model that captures the real structure's behavior as accurately as possible.

Finally, there is another method, namely Ko's displacement theory. This method is suitable for studying the deflection of wings and is based on the Euler-Bernoulli beam theory. Axial deformations along the wing are measured, and the curvatures are easily derived, which, when integrated, generate the deformation. It is also possible to assess the torsion by placing more sensors along a specific chord of the wing.

An example of an analysis performed using Ko's displacement theory for displacements is that concerning the doubly tapered wing of the Ikhana aircraft [37].

Ko's theory was later improved by Pak and allows for the reconstruction of the entire displacement field through a modal reconstruction [38]. It consists of two

steps: the first step involves reconstructing the deformation along the measurement lines, as prescribed by Ko's theory, while the second step enables the reconstruction of the deformation across the entire domain through the modal transformation SEREP [39].

1.3   iFEM method introduction

The iFEM method, which is a shape-sensing method, has several advantages, such as requiring fewer measurements compared to the integration method, and being independent of the shape functions (and thus also of the vibrational modes).

Similar to the standard FEM method, the iFEM method is based on the discretization of a structure using finite elements, in this case, inverse elements. As in the traditional FEM method, the displacement field is reconstructed through the use of shape functions, which, starting from the nodal degrees of freedom, allow the calculation of the degrees of freedom within the element. Additionally, the strain-displacement relations are linear, involving derivatives in space.

The iFEM method uses a functional error that accounts for the difference between calculated and measured deformations. This functional error must be minimized (least squares method) to calculate the displacements, as studied by Tessler and Sprangler in [1], [2].

It follows that the iFEM method depends solely on the geometry of the structure, but not on the operating conditions, nor does it depend on the properties and materials the structure is made of.

The iFEM method was initially implemented for 2-D structures [3], applying Mindlin's kinematic theory [4]. The shell elements that were implemented in this way include the 3-node element iMIN3 [3], the 4-node element iQS4 [5], and the 8-node curved element iCS8 [6].

A limitation of the 2-D iFEM method is that achieving accurate results requires a large number of sensors, and an optimal configuration of these sensors needs to be determined.

The 2-D iFEM method was initially implemented for the study of plates, and later extended to the study of multi-layer composite laminates and sandwich structures [10]. Subsequently, it was extended to the study of wing boxes [11], wing-shaped panels, and shell or stiffened structures [12]. The results of this extension were satisfactory.

The 2-D iFEM method proved to be inaccurate in reconstructing the degrees of freedom of components with a beam or rod shape, where one longitudinal dimension is dominant over the others. As a result, the 1-D iFEM method was implemented by Gherlone et al. [7]. In this case, the kinematic assumptions are those of Timoshenko beam theory, while the functional error to be minimized includes the difference between the longitudinal, bending, shear, and torsional deformations of the beam.

The 1-D iFEM method can be applied, for example, to beam-shaped components, such as stringers and other reinforcements, including circular ones [15], [16].

It is therefore necessary to analyze the advantages and disadvantages of the 1-D and 2-D iFEM methods.

On one hand, the 1-D iFEM method requires fewer sensors and lower computational cost, as it needs fewer elements to model the components. On the other hand, modeling a component with a 1-D element is an approximation, as the reconstructed degrees of freedom are related to the axis of the component, thus neglecting its more complex shape. A component with a complex shape would be inadequately approximated with 1-D elements.

The 2-D iFEM method has the advantage of being more accurate, but at the same time, it requires a greater number of measurements to be precise and higher computational cost.

Therefore, a hybrid 1-D and 2-D method has been implemented to maximize the advantages of both methods [7], [2]. In this case, for example, a wing box can be modeled using 2-D elements (skin, web, ...) and 1-D elements (stringers, ...).

1.4   iFEM Method for non-linear problems

The iFEM method has proven to be accurate in many cases of structures that exhibited small deformations, and therefore, a linear load-displacement relationship. However, when the iFEM method is applied to cases where the structure experiences large deformations, there is a risk that the errors will be significant in predicting the deformed shape.

A first attempt to solve the problem involves creating a "steps" iFEM method, where the deformation of the structure is obtained as the superposition of multiple deformations corresponding to different load steps, under linear assumptions.

The non-linear method that was later implemented is based on the superposition of linear configurations, similar to the method just described.

In the paper [35], there is a study by Tessler, Gherlone et al. that explains the procedure for implementing the non-linear iFEM method and addresses two example problems, one involving a wing-shaped plate and the other a square plate fixed under transverse loading.

The results of this paper clearly indicate that the incremental iFEM approach can be easily implemented as a valid tool for real-time structural health monitoring of aerospace structures subjected to significant deformations.

1.5   Sensors position

To maximize the accuracy and efficiency of shape sensing methods (particularly iFEM), it is important to study the optimal sensor configuration on the structure. A first approach to evaluate this was to introduce penalization strategies for inverse elements that lack deformation data [30]. Examples of cases where the optimal sensor placement has been studied include research on thin-shell cylinders [20], wing-shaped plates [31], and composite wing boxes [26].

In these studies, it is evident that these iterative optimization procedures yielded good results where the structure exhibited simple torsion and bending configurations. However, when the deformation and load fields are more complex, the study

of sensor placement becomes more challenging.

Some studies, such as [32], have addressed this problem, specifically investigating whether there are sensor configurations that guarantee good results universally and systematically in iFEM analysis. In [32], the case study is a simple rectangular panel, and the goal is to examine how different sensor configurations influence the accuracy of displacement reconstruction. The sensor positions are easily reproducible experimentally, and the analyzed cases include both simpler and more complex deformation states. For a better overview, the results were analyzed both at the sensor locations and away from them. Additionally, these operations were carried out considering two types of inverse elements to ensure that the element type did not affect the results.

1.6   Structural Health Monitoring

The most common application for inverse methods in structural analysis is Structural Health Monitoring (SHM) [8], which allows for monitoring the integrity of a structure by measuring deformations (temperature, etc.) in real-time using specialized sensors.

The creation of a digital twin in this case allows for reconstructing the displacement field and thus the deformation of the structure, enabling the determination of stresses and strains in such a way that it becomes possible to monitor, for example, the onset and propagation of damage in the real component. This clearly helps reduce the costs and time of monitoring and analysis, which, if performed manually, would be much higher. An example of this is the study of the phenomenon of aeroelasticity in wings [9], where inverse methods are commonly used.

As reported in [22], structural integrity monitoring has evolved over time, shifting from a preventive to a proactive approach, with continuous and real-time monitoring of specific quantities, such as displacements and deformations.

Especially for aerospace structures, it is challenging to install sensors that are stable and accurate in measuring quantities. However, the recent use of optical fiber has made measurements more accurate, and sensors more stable and less invasive. This is one of the reasons that has led methods like iFEM, which require experimental measurements as input, to develop in live monitoring.

In [36], there is a comparative study that examines the case of a composite wing box using three methods: iFEM, the Modal Method, and Ko's displacement theory, with Pak's update.

2 Inverse Finite Elements Method

The Inverse Finite Element Method (iFEM) has been implemented to analyze different types of structures. In this context, the 1-D iFEM method, suitable for modeling beams and one-dimensional components, and the 2-D iFEM method, suitable for modeling plates and shells, will be studied. Depending on the element, the kinematic relationships underlying the study also vary.

2.1 1-D Inverse Finite Elements Method

A beam with a given cross-section is considered, in the coordinates (x, y, z), where x is the longitudinal axis of the beam, passing through the shear center, while (y, z) are the transverse axes, perpendicular to the beam's axis.

2.1.1 Kinematic Relations

The kinematic relations regarding displacements are those of Timoshenko's beam theory, that is:

$$
\begin{cases}
u_x = u + z\theta_y - y\theta_z \\
u_y = v - z\theta_x \\
u_z = w + y\theta_x
\end{cases}
\tag{1}
$$

where:

- u_x, u_y e u_z are the displacements at a generic point along the x, y, and z axes.

- θ represents the rotation in the three directions.

- u, v, and w are the displacements in the three directions at the shear center.

The strains are obtained through the geometric relations by appropriately differentiating the displacements:

$$
\begin{cases}
\epsilon_x \\
\gamma_{xz} \\
\gamma_{xy}
\end{cases}
=
\begin{cases}
u_{x,x} \\
u_{x,z} + u_{z,x} \\
u_{x,y} + u_{y,x}
\end{cases}
=
\begin{cases}
e_1 + ze_2 + ye_3 \\
e_4 + ye_6 \\
e_5 - ze_6
\end{cases}
$$

where e_i are the longitudinal, bending, torsional, and shear strains of the section along the 3 axes.

The 6 strains e_i are defined as:

$$
e(\mathbf{u}_b) = \{e_1, e_2, e_3, e_4, e_5, e_6\}^T = \{u_{,x}, \theta_{y,x}, -\theta_{z,x}, w_{,x} + \theta_y, v_{,x} - \theta_z, \theta_{x,x}\}^T = \mathbf{B}^s \mathbf{u_b^e}
\tag{2}
$$

where B^s is the matrix of the derivatives of the shape functions and u_b^e is the vector of the nodal degrees of freedom of the element in the inverse model.
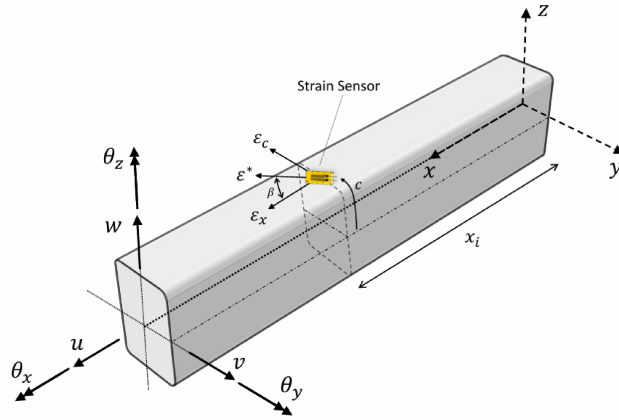
Figure 1: Esempio trave con assi, deformazioni, rotazioni e spostamenti, da [2]

2.1.2 Experimental Strains of the Section

The experimental strains are measured using sensors placed on the beam, specifically strain gauges and optical fibers.

As shown in Figure 1, the angle β is the angle by which the axis of the strain gauge is deviated relative to the beam axis, and x_i are the positions of the sensors. The surface strain at a generic point on a beam, ϵ^*, can be written as a function of the strains e_i:

$$
\begin{aligned}
\epsilon^*(x_i, c, \beta) = {} & \left(e_1^\epsilon(x_i) + e_2^\epsilon(x_i)z(c) + e_3^\epsilon(x_i)y(c)\right)\left(\cos^2(\beta) - \nu \sin^2(\beta)\right) \\
& + \left(\frac{1}{k_{\epsilon z}}e_4^\epsilon(x_i)f_1(c) + \frac{1}{k_{\epsilon y}}e_5^\epsilon(x_i)f_2(c)\right. \\
& \left. + e_6^\epsilon(x_i)f_3(c)\right)\cos(\beta)\sin(\beta)
\end{aligned}
\tag{3}
$$

where f_i are functions that describe the variation of shear strains on the tangential surface due to transverse and torsional loads, c is the circumferential coordinate, and k are coefficients dependent on the beam's cross-sectional profile.

2.1.3 Least Squares Functional Error

The element subdivision is similar to that of classic FEM, however, the analysis procedure includes the presence of a functional to be minimized, defined as:

$$
\mathbf{\Phi_b^e(u_b^e)} \equiv \mathbf{w_s\Phi_s(u_b^e)}
\tag{4}
$$

where w_s is a vector of the coefficients. The vector of functionals $\Phi_s = \{\Phi_e^k\}$ (k=1,...,6) represents the least squares error between the analytical and experimental strains calculated at the N axial sections, and is given by:

$$
\Phi_k^e = \frac{l_e}{N}\sum_{i=1}^{N}\left[e_k(x_i) - (e_k^\epsilon)_i\right]^2
\tag{6}
$$

The weights control the application of the least squares compatibility for each strain component. For an inverse beam element formulated based on Timoshenko's beam

theory, the weight vector $w_s = \{w_k\}$ (k=1,...,6) is given by:

$$w_s = \{w_k\} = \{w_1^0, w_2^0 \frac{I_{yy}}{A_b}, w_3^0 \frac{I_{zz}}{A_b}, w_4^0, w_5^0, w_6^0 \frac{I_t}{A_b}\} \tag{5}$$

where w_k^0 (k=1,...,6) are the dimensionless weight coefficients.

The functional error of the element is solved by minimizing the equation with respect to the nodal degrees of freedom of the element to obtain the following series of linear algebraic equations:

$$\frac{\partial \Phi_b^e(u_b^e)}{\partial u_b^e} = k_b^e u_b^e - f_b^e = 0 \rightarrow k_b^e u_b^e = f_b^e \tag{6}$$

where the matrix k_b^e and the vector f_b^e are analogous to the element stiffness matrix and the force vector in direct FEM. k_b^e is a function only of the sensor positions, while f_b^e is a function of both the sensor positions and the measured strains. These element matrices are the weighted sum of the contributions from each sectional strain term and can be written as:

$$k_b^e(u_b^e) = \sum_{k=1}^{6} w_k \frac{l_e}{N} \sum_{i=1}^{N} (B_k^s(x_i))^T B_k^s(x_i) \tag{7}$$

$$f_b^e(u_b^e) = \sum_{k=1}^{6} w_k \frac{l_e}{N} \sum_{i=1}^{N} (B_k^s(x_i))^T (e_k^\epsilon)_i \tag{8}$$

2.2 2-D Inverse Finite Elements Method

Considering a plate or shell structure defined in the 3-D Cartesian coordinate frame $(x, y, z) \subset \mathbb{R}^3$. The orthogonal coordinates $x \equiv (x, y)$ define the mid-plane of the plate, with the z-axis along the normal to the plane ($z = 0$ defines the surface of the mid-plane). The plate has a thickness of $2t$, where $z \in [-t, t]$, and an area on the mid-plane A_p.

2.2.1 Kinematic Relations

The 2-D FEM for plates or shells is formulated based on the kinematic assumptions of Mindlin's theory. The components of the displacement vector can be described in terms of kinematic variables $\mathbf{u}_p \equiv \{u, v, w, \theta_x, \theta_y\}^T$ as:

$$\begin{cases} u_x = u + z\theta_y \\ u_y = v - z\theta_x \\ u_z = w \end{cases} \tag{9}$$

where u and v are the displacements of the mid-plane surface in the x and y directions; w is the transverse deflection averaged over the thickness of the plate, and θ_x and θ_y are the rotations of the section about the x and y axes.

Using the linear strain-displacement relation, the strain field of the plate is calculated as:

$$\left\{ \begin{array}{c} \epsilon_{xx} \\ \epsilon_{yy} \\ \gamma_{xy} \end{array} \right\} = \left\{ \begin{array}{c} u_{,x} \\ v_{,y} \\ u_{,y} + v_{,x} \end{array} \right\} + z \left\{ \begin{array}{c} \theta_{y,x} \\ -\theta_{x,y} \\ -\theta_{x,x} + \theta_{y,y} \end{array} \right\} = m(\mathbf{u}_p) + zk(\mathbf{u}_p) \qquad (10)$$

where m and k are the strain measures defined on the mid-plane surface of the plate, representing the membrane strains and the curvature of the mid-plane. Similarly, the transverse shear strains are written as:

$$\left\{ \begin{array}{c} \gamma_{xz} \\ \gamma_{yz} \end{array} \right\} = \left\{ \begin{array}{c} u_{z,x} + u_{x,z} \\ u_{z,y} + u_{y,z} \end{array} \right\} = \left\{ \begin{array}{c} w_{,x} + \theta_y \\ w_{,y} - \theta_x \end{array} \right\} = g(\mathbf{u}_p) \qquad (11)$$

where g are the transverse shear strain measures of the plate.
Similarly to the 1-D FEM, the displacements and strains within an element are approximated using the element's shape functions (details in Chapter 3.1):

$$\left\{ \begin{array}{c} \epsilon_{xx} \\ \epsilon_{yy} \\ \gamma_{xy} \end{array} \right\} = m(\mathbf{u}_p^e) + zk(\mathbf{u}_p^e) = B^m \mathbf{u}_p^e + zB^k \mathbf{u}_p^e, \qquad (12)$$

$$\left\{ \begin{array}{c} \gamma_{xz} \\ \gamma_{yz} \end{array} \right\} = g(\mathbf{u}_p^e) = B^g \mathbf{u}_p^e \qquad (13)$$

where B_m is the matrix of the derivatives of the shape functions corresponding to the membrane strains, B_k, is the matrix of the derivatives of the shape functions corresponding to the curvature strains and B_g is the matrix of the derivatives of the shape functions corresponding to the transverse shear strains.
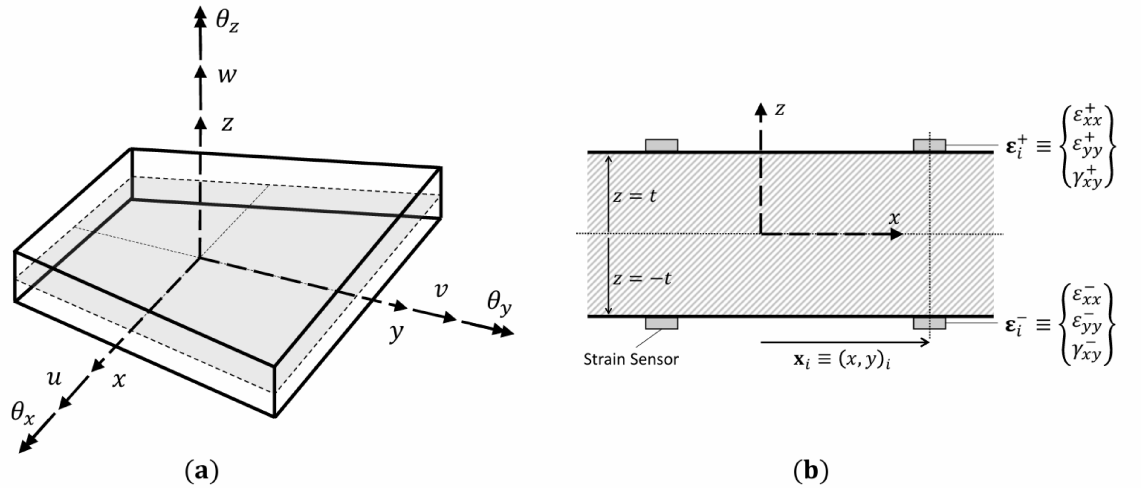$\mathbf{u}_p^e$ is the vector of the nodal degrees of freedom of the element.

Figure 2: Illustration of the plate structure: (a) kinematic variables used to describe the plate deformations and (b) sensors mounted on the upper and lower surfaces of the plate.

2.2.2   Experimental Strain Measurements

The strain measurements in Eq. 13 can be experimentally calculated using strain measurements from sensors mounted on the upper surface ($z = t$) and the lower surface ($z = -t$) of the plate. The sensor positions are defined by $x_i = (x, y)_i$, where $i = 1, \ldots, N$, while the strains measured on the upper and lower surfaces are:

$$\epsilon_i^+ = \left\{ \begin{array}{c} \epsilon_{xx}^+ \\ \epsilon_{yy}^+ \\ \gamma_{xy}^+ \end{array} \right\}_i \quad \text{e} \quad \epsilon_i^- = \left\{ \begin{array}{c} \epsilon_{xx}^- \\ \epsilon_{yy}^- \\ \gamma_{xy}^- \end{array} \right\}_i$$

The surface strain measurements are used to calculate the strain measurements on the mid-surface of the plate using the following relations:

$$m_i^\epsilon = \frac{1}{2} \left(\left\{ \begin{array}{c} \epsilon_{xx}^+ \\ \epsilon_{yy}^+ \\ \gamma_{xy}^+ \end{array} \right\} + \left\{ \begin{array}{c} \epsilon_{xx}^- \\ \epsilon_{yy}^- \\ \gamma_{xy}^- \end{array} \right\} \right)_i, \tag{14}$$

$$k_i^\epsilon = \frac{1}{2t} \left(\left\{ \begin{array}{c} \epsilon_{xx}^+ \\ \epsilon_{yy}^+ \\ \gamma_{xy}^+ \end{array} \right\} - \left\{ \begin{array}{c} \epsilon_{xx}^- \\ \epsilon_{yy}^- \\ \gamma_{xy}^- \end{array} \right\} \right)_i \tag{15}$$

The transverse shear strain measurements cannot be directly calculated from the experimental strains and they are not present in this work.

2.2.3   Least Squares Functional Error

The 2-D iFEM is based on the discretization of the structural domain using inverse finite elements with elemental areas A_p^e. For each inverse element e, a least squares error functional between the analytical and experimental strain measurements is defined as:

$$\Phi_p^e(u_p^e) \equiv w_m \Phi_m(u_p^e) + w_k \Phi_k(u_p^e) + w_g \Phi_g(u_p^e) \tag{16}$$

where w_m, w_k, and w_g are row vectors of weights used to enforce the correlation between the analytical and experimental strain measurements. The error functions, Φ_m, Φ_k, and Φ_g, corresponding to the membrane strain, curvature strain, and transverse shear strain measurements, respectively, are given by:

$$\Phi_m \equiv \frac{1}{A_p^e} \int_{A_p^e} [m(u_p^e) - m^\epsilon]^2 dA, \quad \Phi_k \equiv (2t)^2 \frac{1}{A_p^e} \int_{A_p^e} [k(u_p^e) - k^\epsilon]^2 dA, \tag{17}$$

$$\Phi_g \equiv \frac{1}{A_p^e} \int_{A_p^e} [g(u_p^e) - g^\epsilon]^2 dA \tag{18}$$

If an element have experimental strains, the corresponding weights are set to unity ($w_m = w_k = \{1, 1, 1\}$ and $w_g = \{1, 1\}$), otherwise they are set to a very low value ($10^{-5} - 10^{-3}$). Using a lower weight reduces the contribution of the

element to the global error functional. Since g^ϵ cannot be directly calculated from experimental measurements, the following form is used:

$$\Phi_g \equiv \frac{1}{A_p^e} \int_{A_p^e} [g(u_p^e)]^2 dA \tag{19}$$

where the corresponding weighting coefficient vector is set to a very low value, $w_g = \{10^{-5}, 10^{-5}\}$.
Minimizing equation (16) with respect to the nodal degrees of freedom of the element produces the following set of linear algebraic equations:

$$\frac{\partial \Phi_p^e(u_p^e)}{\partial u_p^e} = k_p^e u_p^e - f_p^e = 0 \Rightarrow k_p^e u_p^e = f_p^e \tag{20}$$

where the matrix k_e^p and the vector f_e^p are given in terms of the derivatives of the shape functions as follows:

$$k_p^e(u_p^e) = \frac{1}{A_p^e} \int_{A_p^e} \left[w_m (B^m)^T B^m + w_k (2t)^2 (B^k)^T B^k + w_g (B^g)^T B^g \right] dA, \tag{21}$$

$$f_p^e(u_p^e) = \frac{1}{A_p^e} \int_{A_p^e} \left[w_m (B^m)^T m^\epsilon + w_k (2t)^2 (B^k)^T k^\epsilon + w_g (B^g)^T g^\epsilon \right] dA. \tag{22}$$

2.3   Hybrid Formulation

The hybrid iFEM formulation combines 1-D and 2-D approaches by discretizing the structure with both inverse beam and shell finite elements. For each beam or shell element, the local element matrices can be related to the global coordinate system using:

$$\{\mathbf{k}_b^e\}_g = (\mathbf{T}^e)^T \mathbf{k}_b^e \mathbf{T}^e, \quad \{\mathbf{f}_b^e\}_g = (\mathbf{T}^e)^T \mathbf{f}_b^e \tag{23}$$

$$\{\mathbf{k}_p^e\}_g = (\mathbf{T}^e)^T \mathbf{k}_p^e \mathbf{T}^e, \quad \{\mathbf{f}_p^e\}_g = (\mathbf{T}^e)^T \mathbf{f}_p^e \tag{24}$$

where the transformation matrix, T^e, accounts for the local orientation of the elements and the offsets with respect to the global coordinate system.
For any node of a beam or plate inverse element, the local degree of freedom can be transformed into the global degree of freedom using the following relations:

$$\begin{bmatrix} u \\ v \\ w \\ \theta_x \\ \theta_y \\ \theta_z \end{bmatrix}_l = \begin{bmatrix} 1 & 0 & 0 & 0 & z_0 & -y_0 \\ 0 & 1 & 0 & -z_0 & 0 & 0 \\ 0 & 0 & 1 & y_0 & 0 & 0 \\ 0 & 0 & 0 & 1 & 0 & 0 \\ 0 & 0 & 0 & 0 & 1 & 0 \\ 0 & 0 & 0 & 0 & 0 & 1 \end{bmatrix} \begin{bmatrix} u \\ v \\ w \\ \theta_x \\ \theta_y \\ \theta_z \end{bmatrix}_g \tag{25}$$

where y_0 and z_0 define the offset of the local axis of the beam element relative to the global structure. Similarly, for shell elements, z_0 is the offset of the mid-surface relative to the global structure (with $y_0 = 0$).

The contributions from all beam and shell elements are assembled using the FEM assembly method to obtain the global system of equations for the structure:

$$\mathbf{KU} = \mathbf{F} \tag{26}$$

As in FEM, boundary conditions ensure a non-singular system matrix. Finally, solving equation (26), iFEM reconstructs the nodal displacements, U, of the structure.

3 Calculation of the displacement and strain field from the nodal degrees of freedom

As in classical FEM, in iFEM it is possible to reconstruct the displacements and strains of an element from the element's nodal degrees of freedom using shape functions.

3.1 Displacement Field in the Inverse Shell Quadrilateral Element

For an inverse quadrilateral element (iQS4), the local coordinates of the element (x, y, z) need to be introduced, with the origin (0, 0, 0) at the centroid of the element, on the midplane, as shown in Figure 3, taken from [20]:
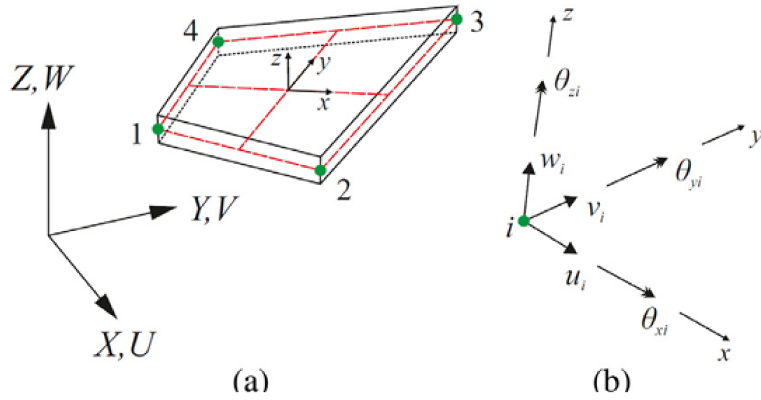
Figure 3: Quadrilateral Element and Local Reference System

It is assumed that the coordinate z is between (z_b, z_t), with z_b and z_t equal and of opposite sign.

In Chapter 3.3, the process of transitioning from local coordinates (x, y, z) to global coordinates (X, Y, Z) is explained.

The coordinates (ξ, η) are the dimensionless coordinates of the element, as shown in Figure 4:

As for the geometry, the equations that allow the calculation of the local coordinates of the element (x, y) in the plane from the node coordinates are:

$$x(\xi, \eta) = \sum_{i=1}^{4} N_i x_i \tag{27}$$

$$y(\xi, \eta) = \sum_{i=1}^{4} N_i y_i \tag{28}$$

where the 8 shape functions are reported below:

$$N_1 = \frac{(1-\xi)(1-\eta)}{4} \tag{29}$$
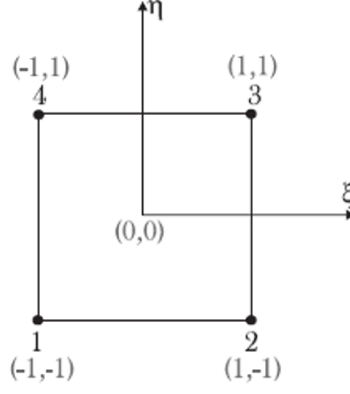
Figure 4: Quadrilateral Element and Dimensionless Local Coordinate System

$$N_2 = \frac{(1+\xi)(1-\eta)}{4} \tag{30}$$

$$N_3 = \frac{(1+\xi)(1+\eta)}{4} \tag{31}$$

$$N_4 = \frac{(1-\xi)(1+\eta)}{4} \tag{32}$$

Each node of the inverse quadrilateral element has 6 degrees of freedom, summarized in the vector u_i^e, that is:

$$u_i^e \equiv \{u_i, v_i, w_i, \theta_{xi}, \theta_{yi}, \theta_{zi}\}^T \tag{33}$$

where u_i, v_i, w_i are the displacements in the x, y, and z directions, respectively, while θ_{xi}, θ_{yi}, and θ_{zi} are the rotations.

At this point, it is possible to define the membrane displacements in the xy-plane, namely u and v, using shape functions and nodal values, as follows:

$$u(x,y) = \sum_{i=1}^{4} N_i u_i + \sum_{i=1}^{4} L_i \theta_{zi} \tag{34}$$

$$v(x,y) = \sum_{i=1}^{4} N_i v_i + \sum_{i=1}^{4} M_i \theta_{zi} \tag{35}$$

The transverse displacement and the out-of-plane rotations, namely w, θ_x, and θ_y, are calculated as follows, using the anisoparametric shape functions developed by Tessler and Hughes in [21] for the MIN4 element (which is based on Mindlin's theory):

$$w(x,y) = \sum_{i=1}^{4} N_i w_i - \sum_{i=1}^{4} L_i \theta_{xi} - \sum_{i=1}^{4} M_i \theta_{yi} \tag{36}$$

$$\theta_x(x,y) = \sum_{i=1}^{4} N_i \theta_{xi} \tag{37}$$

17

$$\theta_y(x, y) = \sum_{i=1}^{4} N_i \theta_{yi} \tag{38}$$

where L_i and M_i are the shape functions that relate the in-plane rotation θ_z and the displacements in the plane u and v. The functions L_i and M_i are given below:

$$L_1 = y_{14} N_8 - y_{21} N_5 \tag{39}$$

$$L_2 = y_{21} N_5 - y_{32} N_6 \tag{40}$$

$$L_3 = y_{32} N_6 - y_{43} N_7 \tag{41}$$

$$L_4 = y_{43} N_7 - y_{14} N_8 \tag{42}$$

$$M_1 = x_{41} N_8 - x_{12} N_5 \tag{43}$$

$$M_2 = x_{12} N_5 - x_{23} N_6 \tag{44}$$

$$M_3 = x_{23} N_6 - x_{34} N_7 \tag{45}$$

$$M_4 = x_{34} N_7 - x_{41} N_8 \tag{46}$$

where:

$$N_5 = \frac{(1 - \xi^2)(1 - \eta)}{16} \tag{47}$$

$$N_6 = \frac{(1 + \xi)(1 - \eta^2)}{16} \tag{48}$$

$$N_7 = \frac{(1 - \xi^2)(1 + \eta)}{16} \tag{49}$$

$$N_8 = \frac{(1 - \xi)(1 - \eta^2)}{16} \tag{50}$$

$$x_{ij} = x_i - x_j \tag{51}$$
$$y_{ij} = y_i - y_j \tag{52}$$

with i,j = 1,2,3,4.
Using these equations, the three displacement components u_x, u_y, u_z along the three axes (x, y, z) for each point of the element can be written as follows:

$$u_x(x, y, z) = u + z\theta_y \tag{53}$$

18

$$u_y(x, y, z) = v - z\theta_x \tag{54}$$

$$u_z(x, y, z) = w \tag{55}$$

Where u_x and u_y are the in-plane displacement components and u_z is the transverse displacement component.

3.2 Strain Field in the Inverse Shell Quadrilateral Element

The linear displacement-strain relations are as follows:

$$\epsilon_{xx} = \frac{\partial u_x}{\partial x} = \frac{\partial u}{\partial x} + z\frac{\partial \theta_y}{\partial x} \tag{56}$$

$$\epsilon_{yy} = \frac{\partial u_y}{\partial y} = \frac{\partial v}{\partial y} - z\frac{\partial \theta_x}{\partial y} \tag{57}$$

$$\gamma_{xy} = \frac{\partial u_y}{\partial x} + \frac{\partial u_x}{\partial y} = \frac{\partial v}{\partial x} + \frac{\partial u}{\partial y} + z\left(\frac{\partial \theta_y}{\partial y} - \frac{\partial \theta_x}{\partial x}\right) \tag{58}$$

$$\gamma_{xz} = \frac{\partial u_z}{\partial x} + \frac{\partial u_x}{\partial z} = \frac{\partial w}{\partial x} + \theta_y \tag{59}$$

$$\gamma_{yz} = \frac{\partial u_z}{\partial y} + \frac{\partial u_y}{\partial z} = \frac{\partial w}{\partial y} - \theta_x \tag{60}$$

It should be noted that the plane stress assumption implies that $\epsilon_{zz} = 0$.
It is also noted that by differentiating the displacements and rotations in space, the shape functions are also differentiated in space. Below are the derivatives of the shape functions with respect to the local dimensionless coordinates (ξ, η):

$$N_{1,\xi} = -\frac{1}{4}(1 - \eta) \tag{61}$$

$$N_{2,\xi} = \frac{1}{4}(1 - \eta) \tag{62}$$

$$N_{3,\xi} = \frac{1}{4}(1 + \eta) \tag{63}$$

$$N_{4,\xi} = -\frac{1}{4}(1 + \eta) \tag{64}$$

$$N_{5,\xi} = -\frac{1}{8}\xi(1 - \eta) \tag{65}$$

$$N_{6,\xi} = \frac{1}{16}(1 - \eta^2) \tag{66}$$

$$N_{7,\xi} = -\frac{1}{8}\xi(1 + \eta) \tag{67}$$

$$N_{8,\xi} = -\frac{1}{16}(1 - \eta^2) \tag{68}$$

$$N_{1,\eta} = -\frac{1}{4}(1 - \xi) \tag{69}$$

$$N_{2,\eta} = -\frac{1}{4}(1 + \xi) \tag{70}$$

$$N_{3,\eta} = \frac{1}{4}(1 + \xi) \tag{71}$$

$$N_{4,\eta} = \frac{1}{4}(1 - \xi) \tag{72}$$

$$N_{5,\eta} = -\frac{1}{16}(1 - \xi^2) \tag{73}$$

$$N_{6,\eta} = -\frac{1}{8}\eta(1 + \xi) \tag{74}$$

$$N_{7,\eta} = \frac{1}{16}(1 - \xi^2) \tag{75}$$

$$N_{8,\eta} = -\frac{1}{8}\eta(1 - \xi) \tag{76}$$

$$M_{1,\xi} = \frac{1}{8}\left(-x_{41}(\frac{1}{2}(1 - \eta^2)) + x_{12}(\xi(1 - \eta))\right) \tag{77}$$

$$M_{2,\xi} = \frac{1}{8}\left(-x_{12}(\xi(1 - \eta)) - x_{23}(\frac{1}{2}(1 - \eta^2))\right) \tag{78}$$

$$M_{3,\xi} = \frac{1}{8}\left(x_{23}(\frac{1}{2}(1 - \eta^2) + x_{34}\xi(1 + \eta))\right) \tag{79}$$

$$M_{4,\xi} = \frac{1}{8}\left(-x_{34}(\xi(1 + \eta)) + x_{41}(\frac{1}{2}(1 - \eta^2))\right) \tag{80}$$

$$M_{1,\eta} = \frac{1}{8}\left(-x_{41}(\eta(1 - \xi)) + x_{12}(\frac{1}{2}(1 - \xi^2))\right) \tag{81}$$

$$M_{2,\eta} = \frac{1}{8}\left(-x_{12}(\frac{1}{2}(1 - \xi^2)) + x_{23}(\eta(1 + \xi))\right) \tag{82}$$

$$M_{3,\eta} = \frac{1}{8}\left(-x_{23}(\eta(1 + \xi)) - x_{34}(\frac{1}{2}(1 - \xi^2))\right) \tag{83}$$

$$M_{4,\eta} = \frac{1}{8}\left(x_{34}(\frac{1}{2}(1 - \xi^2)) + x_{41}(\eta(1 - \xi))\right) \tag{84}$$

$$L_{1,\xi} = \frac{1}{8}\left(-y_{14}(\frac{1}{2}(1 - \eta^2)) + y_{21}(\xi(1 - \eta))\right) \tag{85}$$

$$L_{2,\xi} = \frac{1}{8}\left(-y_{21}(\xi(1 - \eta) - y_{32}(\frac{1}{2}(1 - \eta^2))\right) \tag{86}$$

$$L_{3,\xi} = \frac{1}{8}\left(y_{32}(\frac{1}{2}(1 - \eta^2)) + y_{43}(\xi(1 + \eta))\right) \tag{87}$$

$$L_{4,\xi} = \frac{1}{8}\left(-y_{43}(\xi(1+\eta)) + y_{14}(\frac{1}{2}(1-\eta^2))\right) \tag{88}$$

$$L_{1,\eta} = \frac{1}{8}\left(-y_{14}(\eta(1-\xi)) + y_{21}(\frac{1}{2}(1-\xi^2))\right) \tag{89}$$

$$L_{2,\eta} = \frac{1}{8}\left(-y_{21}(-\frac{1}{2}(1-\xi^2)) + y_{32}(\eta(1+\xi))\right) \tag{90}$$

$$L_{3,\eta} = \frac{1}{8}\left(-y_{32}(\eta(1+\xi)) - y_{43}(\frac{1}{2}(1-\xi^2))\right) \tag{91}$$

$$L_{4,\eta} = \frac{1}{8}\left(y_{43}(\frac{1}{2}(1-\xi^2)) + y_{14}(\eta(1-\xi))\right) \tag{92}$$

Associated with the change of coordinates from global to local is a Jacobian matrix J. In general, the *Jacobian matrix* of a vector-valued function $\mathbf{f} : \mathbb{R}^n \to \mathbb{R}^m$, with $\mathbf{f} = (f_1, f_2, \ldots, f_m)$, is the matrix of partial derivatives of $\mathbf{f}$ with respect to the variables $\mathbf{x} = (x_1, x_2, \ldots, x_n)$. It is defined as follows:

$$J(\mathbf{f}) = \begin{pmatrix} \frac{\partial f_1}{\partial x_1} & \frac{\partial f_1}{\partial x_2} & \cdots & \frac{\partial f_1}{\partial x_n} \\ \frac{\partial f_2}{\partial x_1} & \frac{\partial f_2}{\partial x_2} & \cdots & \frac{\partial f_2}{\partial x_n} \\ \vdots & \vdots & \ddots & \vdots \\ \frac{\partial f_m}{\partial x_1} & \frac{\partial f_m}{\partial x_2} & \cdots & \frac{\partial f_m}{\partial x_n} \end{pmatrix}$$

where the element in the i-th row and j-th column is the partial derivative of f_i with respect to x_j, i.e. $\frac{\partial f_i}{\partial x_j}$.

In this case, the elements that make up the Jacobian matrix (2x2) that transforms the coordinates (ξ, η) into (x, y) are:

$$J_{11} = \frac{1}{4}\left(x_{21}(1-\eta) + x_{34}(1+\eta)\right) \tag{93}$$

$$J_{12} = \frac{1}{4}\left(y_{21}(1-\eta) + y_{34}(1+\eta)\right) \tag{94}$$

$$J_{21} = \frac{1}{4}\left(x_{41}(1-\xi) + x_{32}(1+\xi)\right) \tag{95}$$

$$J_{22} = \frac{1}{4}\left(y_{41}(1-\xi) + y_{32}(1+\xi)\right) \tag{96}$$

while the determinant Δ_J is given by:

$$\Delta J = J_{11}J_{22} - J_{12}J_{21} \tag{97}$$

To calculate the derivatives with respect to x and y, the Jacobian matrix J must be used, and in particular, the inverse matrix I_J, whose elements are:

$$I_{J_{11}} = \frac{J_{22}}{\Delta J} \tag{98}$$

$$I_{J_{12}} = -\frac{J_{12}}{\Delta J} \tag{99}$$

$$I_{J_{21}} = -\frac{J_{21}}{\Delta J} \tag{100}$$

$$I_{J_{22}} = \frac{J_{11}}{\Delta J} \tag{101}$$

The derivatives of the shape functions with respect to x and y are then obtained as:

$$N_{r,x} = I_{J_{11}} N_{r,\xi} + I_{J_{12}} N_{r,\eta} \tag{102}$$

$$N_{r,y} = I_{J_{21}} N_{r,\xi} + I_{J_{22}} N_{r,\eta} \tag{103}$$

$$M_{k,x} = I_{J_{11}} M_{k,\xi} + I_{J_{12}} M_{k,\eta} \tag{104}$$

$$M_{k,y} = I_{J_{21}} M_{k,\xi} + I_{J_{22}} M_{k,\eta} \tag{105}$$

$$L_{k,x} = I_{J_{11}} L_{k,\xi} + I_{J_{12}} L_{k,\eta} \tag{106}$$

$$L_{k,y} = I_{J_{21}} L_{k,\xi} + I_{J_{22}} L_{k,\eta} \tag{107}$$

with k=1,2,3,4 and r=1,2,3,4,5,6,7,8.

Once the derivatives of the shape functions are obtained, it is possible to construct the shape function derivative matrices, resulting in the following expressions for the in-plane deformations:

$$\begin{pmatrix} \epsilon_{xx} \\ \epsilon_{yy} \\ \gamma_{xy} \end{pmatrix} = m(u_p^e) + zk(u_p^e) = B_m u_p^e + zB_k u_p^e, \tag{108}$$

For each element, there is a matrix B_e given by:

$$B_e = B_m + z_t B_k. \tag{109}$$

Here, only the top coordinate has been considered, and the same operation must be performed for the bottom coordinate.

3.3 Rotation of the Reference System

It is necessary to analyze how to reconcile the local reference systems of the elements with the global reference system.

This procedure requests a tensor of size $(3x3xn_e)$, which contains a 3x3 matrix for each element of the model. Each 3x3 matrix, which can be called, for example, "Rot", is of the form:

$$\mathbf{Rot} = \begin{bmatrix} i_1 & j_1 & k_1 \\ i_2 & j_2 & k_2 \\ i_3 & j_3 & k_3 \end{bmatrix}$$

This matrix contains, for each row, the 3 coordinates in the global reference system of the 3 axes of the local reference system of the element.

If the local reference system of an element and the global one are aligned, the resulting matrix is the identity matrix:

$$\mathbf{Rot} = \begin{bmatrix} 1 & 0 & 0 \\ 0 & 1 & 0 \\ 0 & 0 & 1 \end{bmatrix}$$

Each "Rot" matrix for each element must be expanded to be multiplied by B^e. Thus, an expanded matrix Rot_{exp} of dimension 24×24 must be created, which has 8 submatrices "Rot" along its diagonal.

Therefore, Rot_{exp} must multiply B^e, and a matrix is obtained, which can be called, for example, B^r:

$$B^r = B^e * Rot_{exp} \tag{110}$$

At this point, each element is associated with a matrix B^r that takes into account the derivatives of the shape functions and the variation between the orientation of the local and global reference systems.

For each element, the matrix B^r becomes a sub-matrix that contributes to some parts of the matrix M.

The key logical step is that the matrix B^r has 24 columns, which must be multiplied by 24 degrees of freedom. These 24 degrees of freedom are grouped in such a way that there are 6 degrees of freedom for 4 nodes, i.e., 4 groups of 6 degrees of freedom. The 4 groups, or 4 nodes, are the 4 nodes of each element and are arranged in sequence to respect the Connectivity Matrix.

This is a matrix of size $(n_e \times 5)$ that associates each element with its corresponding 4 nodes in a counterclockwise direction, always starting from the node with local coordinates (-1,-1).

The 6 consecutive columns corresponding to a node in the matrix B^r are copied into the positions in M corresponding to the same node. The correspondence between the node in B^r and in M is achieved through the Connectivity Matrix. This operation must be performed for each element, and in this way, the degrees of freedom on the columns of the matrix M are obtained without node repetition. Obviously, this operation must be done for both the top and bottom B^r matrices.

As for the rows of M, each element occupies (27×2) rows of M, since 27 is the size of the rows of a single matrix B^r, and 2 represents the top and bottom.

Thus, a matrix M is obtained which has $(27 \times 2 \times n_e)$ rows. The number of rows that we want to obtain in the matrix M is $(9 \times 3 \times 2 \times n_e)$, as explained previously, and it is immediately evident that the two numbers match.

The matrix M has $(6 \times n_n)$ columns, as expected, corresponding to the 6 degrees

of freedom for each node, arranged in increasing order of identification number. Thus, we can write:

$$\epsilon_g = M * q \tag{111}$$

The vector ϵ_g contains 54 strains for each element, 27 top and 27 bottom. Each of these 27 is grouped as 9×3, i.e., the 9 ϵ_{xx} strains at the 9 Gauss points of the element, the 9 ϵ_{yy} strains at the 9 Gauss points of the element, and the 9 ϵ_{xy} strains at the 9 Gauss points of the element.
In each group of 9 strains corresponding to the 9 Gauss points the fifth position corresponds to the strain at the centroid of the element.

3.4   Calculation of Strains at the Nodes

The goal now is to calculate the strains at the 4 nodes of the element, given the strains at the 9 Gauss points.
First, two reference systems must be defined, as shown in Figure 5.
The first reference system is the element's local coordinate system (ξ,η), already known, while the second is the local coordinate system of the fictitious element whose nodes are the Gauss points, i.e., the coordinate system (ξ',η').
It should be noted that in Figure 5 the calculation method was performed using only 4 Gauss points, whereas in this case, 9 Gauss points are used. However, Figure 5 is only intended to conceptually explain the difference between the two reference systems.
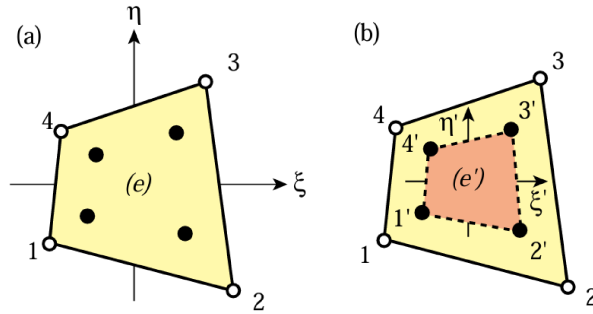
Figure 5: Comparison of reference systems

In the case of 9 Gauss points, the coordinates of the 4 nodes in the reference system (ξ',η') can be written as:

$$\xi'_1 = -\sqrt{5/3}, \eta'_1 = -\sqrt{5/3} \tag{112}$$

$$\xi'_2 = \sqrt{5/3}, \eta'_2 = -\sqrt{5/3} \tag{113}$$

$$\xi'_3 = \sqrt{5/3}, \eta'_3 = \sqrt{5/3} \tag{114}$$

$$\xi'_4 = -\sqrt{5/3}, \eta'_4 = \sqrt{5/3} \tag{115}$$

It can be observed that the node coordinates in this case are greater than 1. Figure 6 shows an 8-node element with 9 Gauss points, and the illustration is easily adaptable to the case with 4 nodes.
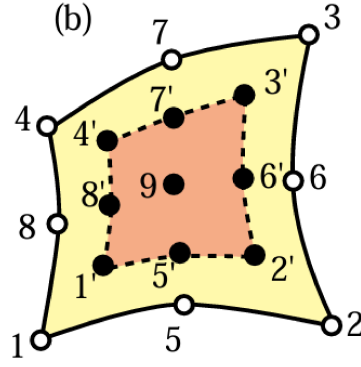
Figure 6: Elemento a 8 nodi e 9 punti di Gauss

3.5 Biquadratic Functions

To calculate the strains at the 4 nodes from the strains at the 9 Gauss points, 9 biquadratic shape functions are used:

$$P_1 = \frac{1}{4}(\xi' - 1)(\eta' - 1)\xi'\eta' \tag{116}$$

$$P_2 = \frac{1}{4}(1 + \xi')(\eta' - 1)\xi'\eta' \tag{117}$$

$$P_3 = \frac{1}{4}(1 + \xi')(1 + \eta')\xi'\eta' \tag{118}$$

$$P_4 = \frac{1}{4}(\xi' - 1)(1 + \eta')\xi'\eta' \tag{119}$$

$$P_5 = \frac{1}{2}(1 - \xi'^2)(\eta' - 1)\eta' \tag{120}$$

$$P_6 = \frac{1}{2}(1 - \xi'^2)(\eta' + 1)\eta' \tag{121}$$

$$P_7 = \frac{1}{2}(\xi' - 1)(1 - \eta'^2)\xi' \tag{122}$$

$$P_8 = \frac{1}{2}(\xi' + 1)(1 - \eta'^2)\xi' \tag{123}$$

$$P_9 = (1 - \xi'^2)(1 - \eta'^2) \tag{124}$$

Where ξ' and η' are, as previously described, the coordinates of the 4 nodes in the local coordinate system of the element with vertices at the Gauss points. Thus, a matrix P of size (4x9) is obtained such that:

$$P = \begin{bmatrix} P_1(\xi_1',\eta_1') & P_2(\xi_1',\eta_1') & P_3(\xi_1',\eta_1') & P_4(\xi_1',\eta_1') & P_5(\xi_1',\eta_1') & P_6(\xi_1',\eta_1') & P_7(\xi_1',\eta_1') & P_8(\xi_1',\eta_1') & P_9(\xi_1',\eta_1') \\ P_1(\xi_2',\eta_2') & P_2(\xi_2',\eta_2') & P_3(\xi_2',\eta_2') & P_4(\xi_2',\eta_2') & P_5(\xi_2',\eta_2') & P_6(\xi_2',\eta_2') & P_7(\xi_2',\eta_2') & P_8(\xi_2',\eta_2') & P_9(\xi_2',\eta_2') \\ P_1(\xi_3',\eta_3') & P_2(\xi_3',\eta_3') & P_3(\xi_3',\eta_3') & P_4(\xi_3',\eta_3') & P_5(\xi_3',\eta_3') & P_6(\xi_3',\eta_3') & P_7(\xi_3',\eta_3') & P_8(\xi_3',\eta_3') & P_9(\xi_3',\eta_3') \\ P_1(\xi_4',\eta_4') & P_2(\xi_4',\eta_4') & P_3(\xi_4',\eta_4') & P_4(\xi_4',\eta_4') & P_5(\xi_4',\eta_4') & P_6(\xi_4',\eta_4') & P_7(\xi_4',\eta_4') & P_8(\xi_4',\eta_4') & P_9(\xi_4',\eta_4') \end{bmatrix}$$

The matrix P must be multiplied by a vector of strains at the 9 Gauss points to obtain the strains at the 4 nodes. The following equation is then obtained:

25

$$\epsilon_{xxn} = P * \epsilon_{xxg} \tag{125}$$

$$\epsilon_{yyn} = P * \epsilon_{yyg} \tag{126}$$

$$\gamma_{xyn} = P * \epsilon_{xyg} \tag{127}$$

where ϵ_{xxn} is a 4x1 vector containing the strains along the x-axis calculated at the 4 nodes, and ϵ_{xxg} is a 9x1 vector containing the strains along the x-axis calculated at the 9 Gauss points. The same applies for the strains along the y-axis and in the xy-plane.

3.6   Strains at Coincident Nodes

The 9 Gauss points are unique and vary from element to element, but this is not the case for the nodes. In fact, two adjacent QUAD4 elements share 2 common nodes, or it may happen that 4 QUAD elements share 4 coincident nodes.

The issue arises from the fact that strains at the nodes are calculated from the strains at the Gauss points, element by element. Therefore, it is possible for the same node, which is shared by multiple elements, to have different strain values.

To resolve this issue, it has been decided to simply average the strain values between the elements at the node:

$$\epsilon_{xxni} = \sum_{i=1}^{n} (\epsilon_{xxnie})/n \tag{128}$$

where i denotes the i-th node, e denotes the element that contains the i-th node, and n represents the number of coincident nodes, so in this case $n = 1, 2, 3, 4$.

4 Numerical Validation with the Simplified Model

Before proceeding with the analysis of the real structure, a preliminary analysis was conducted on a simplified iFEM model representing a panel.

4.1 Panel with the Local Coordinate System Coinciding with the Global One

This model, which can be visualized in the MSC.Patran software in Figure 7, is a simple rectangular panel composed of 2-D laminated shell elements. Each element is characterized by a local coordinate system that coincides with the global one. As a result, the matrix Rot obtained for each element is the identity matrix:

$$\mathbf{Rot} = \begin{bmatrix} 1 & 0 & 0 \\ 0 & 1 & 0 \\ 0 & 0 & 1 \end{bmatrix}$$
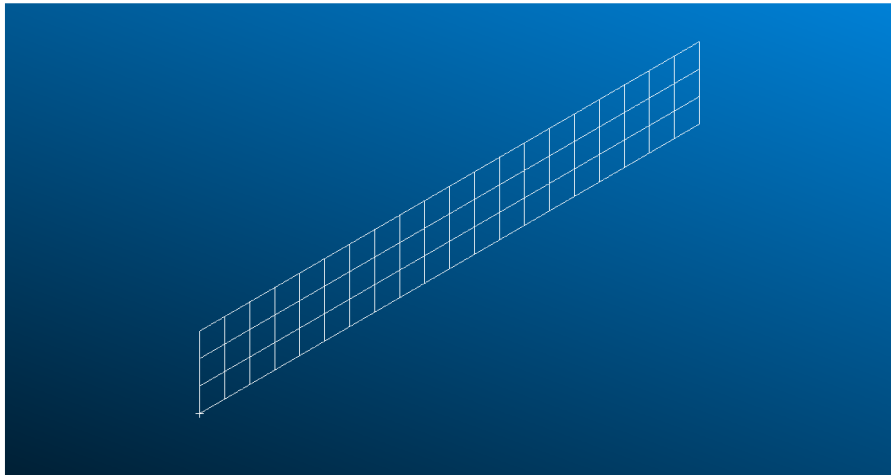
Figure 7: Representation of the simplified panel model

This panel is entirely composed of 2-D laminated elements made of ERGAL aluminum alloy, assumed to be isotropic, with a Young's modulus of E=67545 MPa and a Poisson's ratio of ν=0.33.

The panel is constrained at one end with a fixed support that blocks all degrees of freedom, and two loads of intensity equal to 10 N are applied, as shown in Figure 8:

A structural analysis was performed, which allowed the calculation of displacements and rotations at the nodes, i.e., the nodal degrees of freedom that serve as input for the strain calculation code.

Then, using as input the degrees of freedom obtained from the analysis of the Abaqus FEA software, strains along the x and y axes and rotation in the xy plane were obtained, both at the z_t and z_b levels, through the procedure previously outlined.

This phase is crucial as it helps verify whether the strain calculation code is accurate or not. For comparison, the strains calculated by the Abaqus FEA software
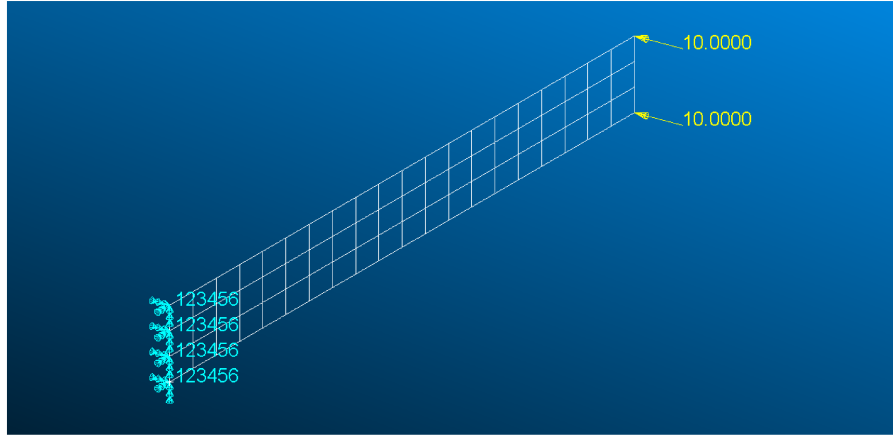
Figure 8: Representation of the simplified panel model with constraints and loads

were used as a reference.

To make a comparison, the relative error between the strains calculated at the centroids of the elements was computed.

For example, considering the relative errors between the strains along the x-axis (ϵ_{xx}) at the centroids calculated with the calculation procedure and those computed by the solver, a vector of 60 elements is obtained, since the number of elements is 60, which is shown below in Figure 9:
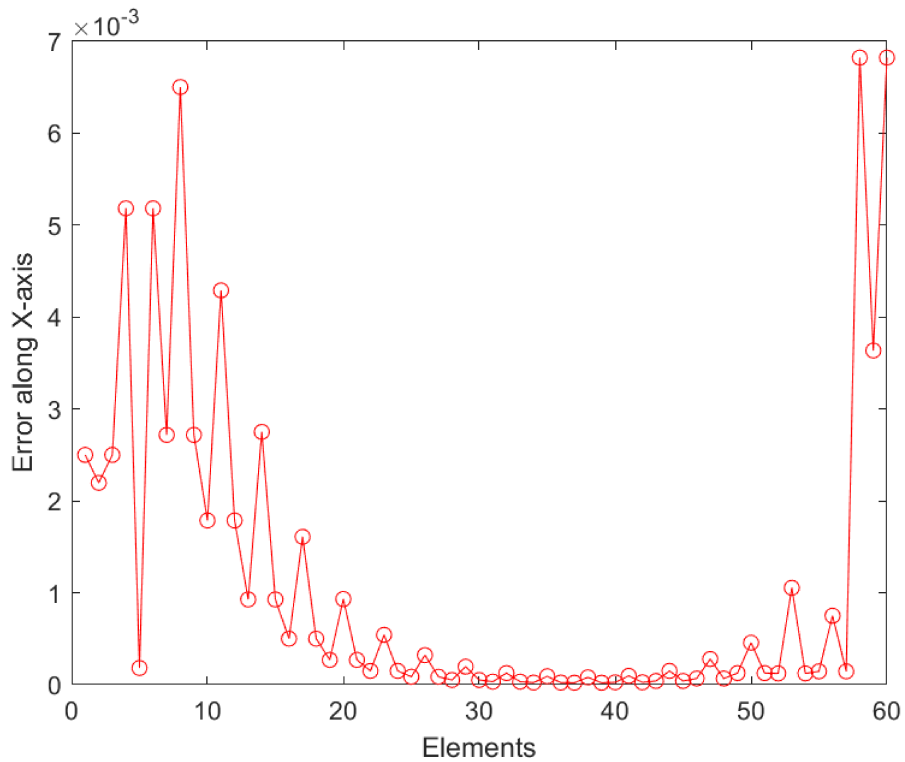
Figure 9: Relative error of the strains along the x-axis

It can be noted that the relative error between the ϵ_{xx} does not exceed 0.7%. Therefore, it can be concluded that the approximation is excellent, and the strains ϵ_{xx} calculated with the code are very similar to those calculated by the Abaqus

software.

Figures 10 and 11 show the errors for the strains along the y-axis (ϵ_{yy}) and in the xy-plane (ϵ_{xy}):
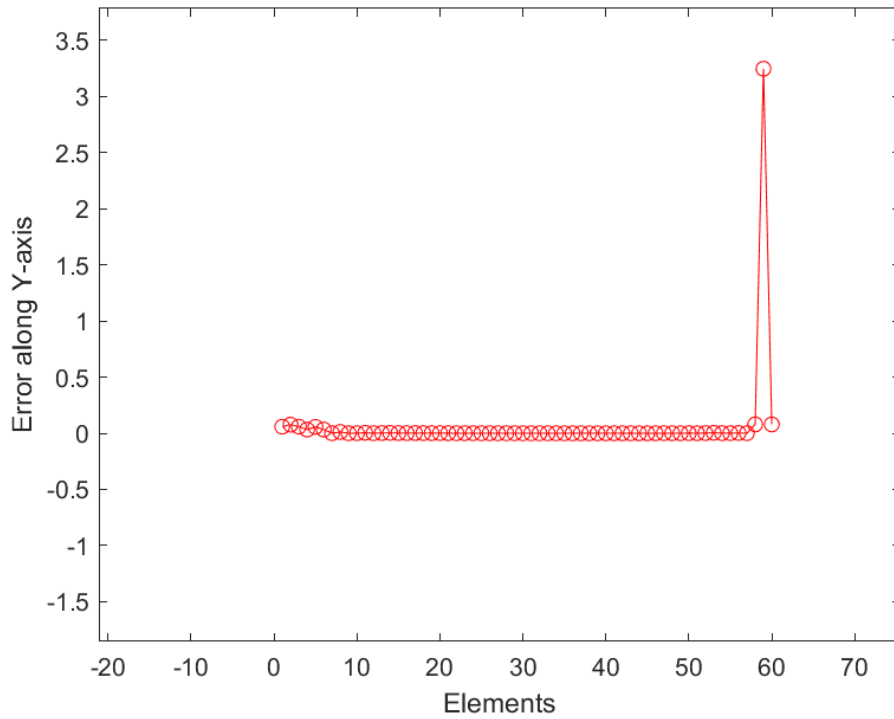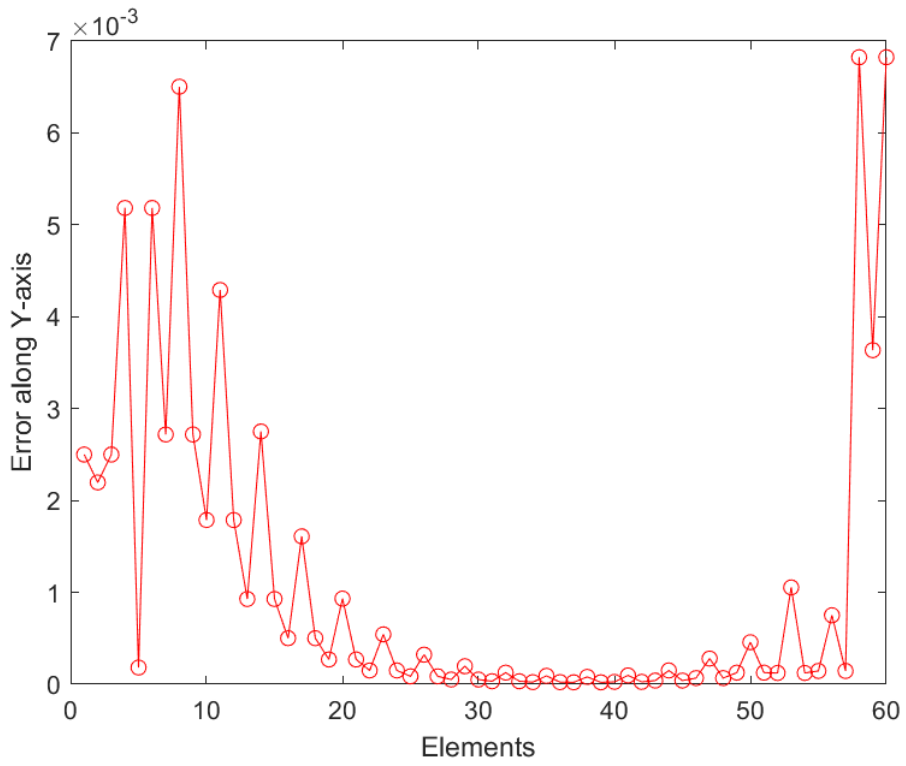

Figure 10: Relative error of the strains along the y-axis
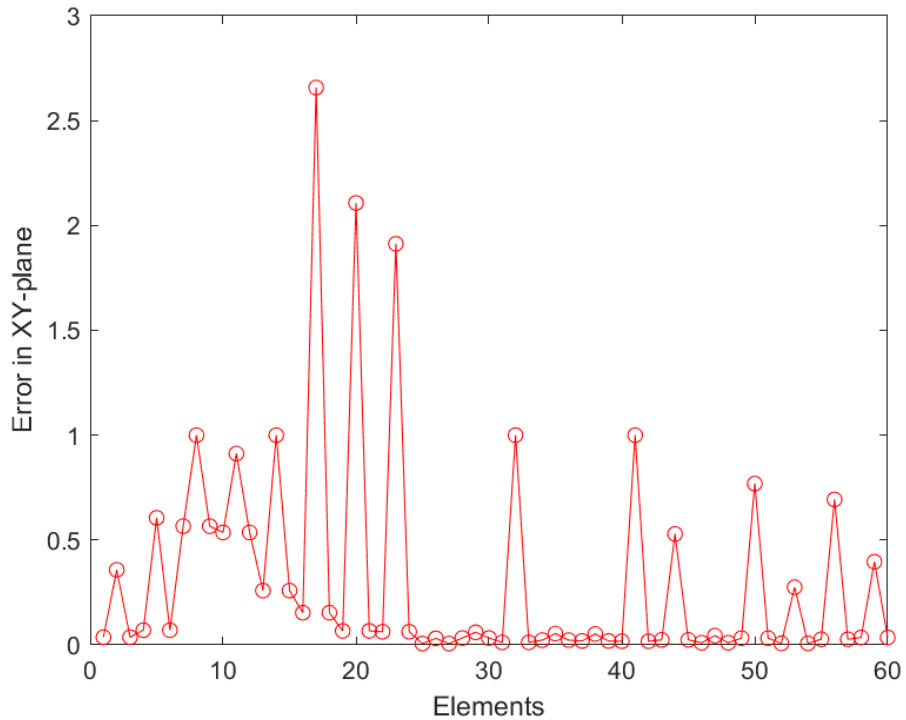
Figure 11: Relative error of the rotation strains in the xy-plane

It is evident that the error is close to 0, with a peak error of 300% for element 59. However, this high error is justified, as the strain calculated by the Abaqus

software is -2.45e-07, while the analytically calculated strain is -5.50e-07. The magnitudes involved are infinitesimal, so the relative error can be very high even if the absolute error is minimal.

The same reasoning applies to other elements, both for ϵ_{yy} and ϵ_{xy}, as in these two cases the magnitudes are often between 1e-5 and 1e-7.

It can be observed that the errors are even higher for ϵ_{xy}, but the magnitudes for ϵ_{xy} are even more infinitesimal than for ϵ_{yy}. For example, the two strains for element 17 are -8.73e-12 and 5.26e-12, confirming the previous statement.

4.2 Panel with the Local Reference System Rotated with respect to the Global One

Considering the same panel, but with a local reference system for each element rotated by 90° with respect to the global one, the results should be the same. The strain results should be equal in magnitude to the previous case, but in this case, the axes corresponding to the various quantities will change. For example, the (ϵ_{xx}) from the previous case will become (ϵ_{yy}) in this case.

The panel with the local reference systems is shown in Figure 12:
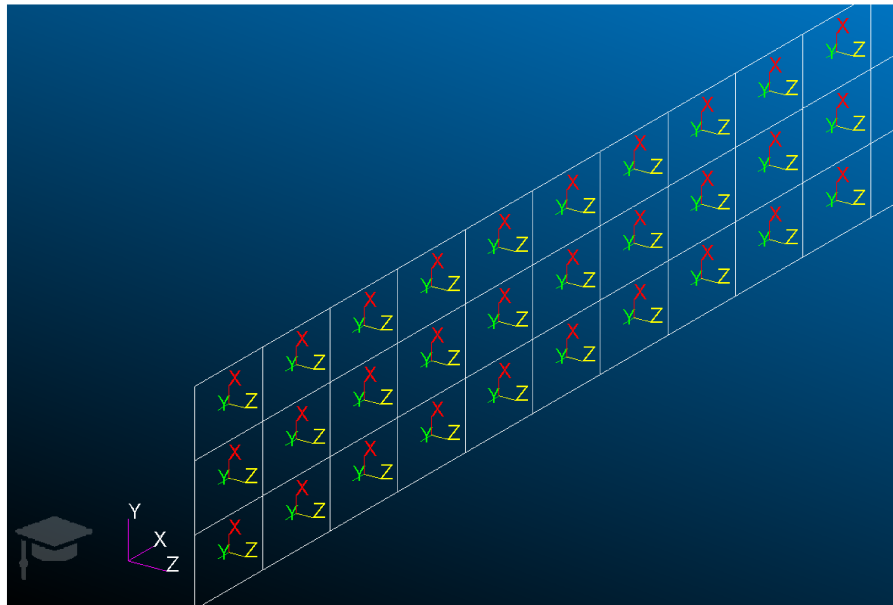
Figure 12: Simplified model of the panel with the local rotated reference systems of the elements

In this case, the rotation matrices Rot of the elements are generally different from the identity matrix.

By analyzing the results, shown in Figures 13, 14, and 15, it is noticeable that the graphs are exactly the same as in the case of the panel with the local reference systems coincident with the global one, but the x and y axes are inverted:

The considerations are the same as those previously mentioned, and it should be noted how this was made possible thanks to the rotation matrices of the reference systems, as discussed in Chapter 3.3.
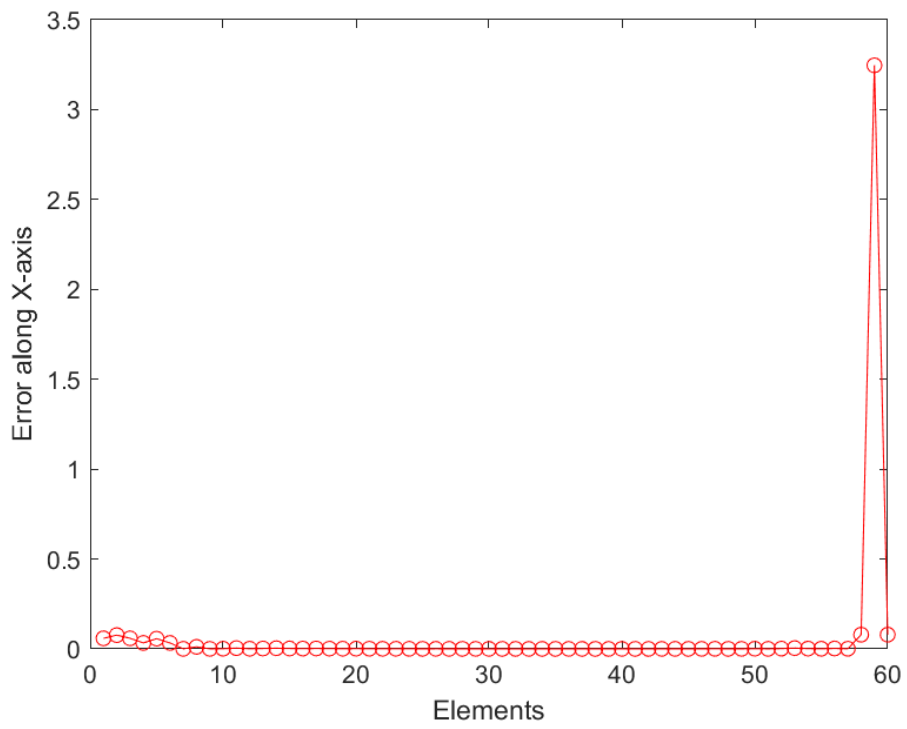
Figure 13: Relative error of the strains along the x-axis

Figure 14: Relative error of the strains along the y-axis
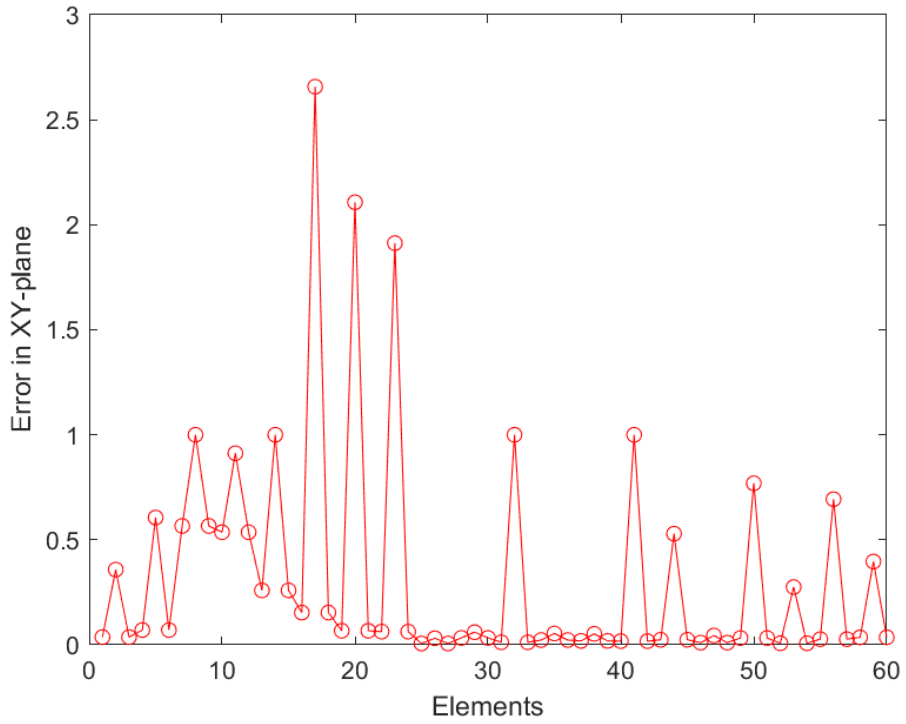
Figure 15: Relative error of the strains in the xy plane

5 Experimental Validation

The experimental validation was carried out on a composite stiffened panel in the shape of a wing, where displacements and strains were measured. These strains will be provided as input to the iFEM software. Finally, it is important to verify the differences between the reconstructed strains and the measured strains.

5.1 Experimental Setup

The object of study is a composite panel representing a wing, stiffened with stringers, as shown in Figure 16.
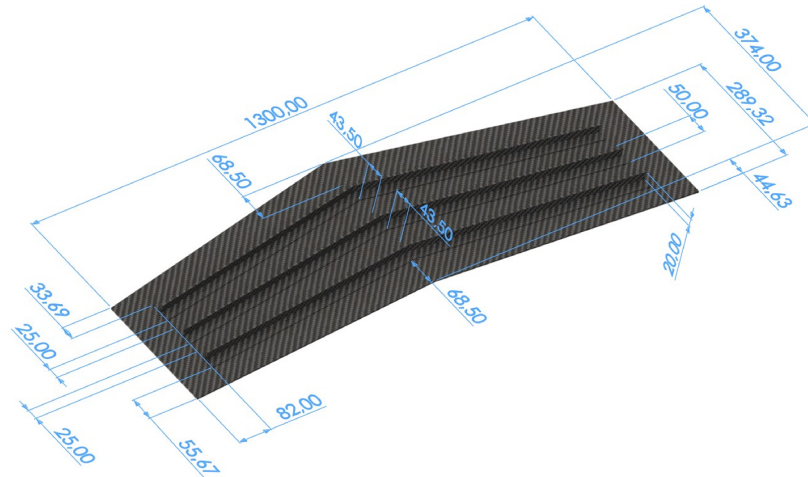
Figure 16: Representation of the composite panel

The entire structure is made of a multi-layer composite, with layers consisting of a carbon fiber fabric prepreg, TWILLT-300. The characteristics of the prepreg are shown in Figure 19. The stacking sequence of the panel and the web of the stringers is [45/0/0/45/0/0/0/45]s, according to the reference guidelines shown in Figure 18. The T-shaped stringers are made by bending the web layers at a 90° angle to obtain the two caps, which are then bonded to the panel. Therefore, the stacking sequence of each cap is derived from the bending of half of the web's stacking sequence.

5.2 Test

5.2.1 Loading and Constraints

The experimental setup is schematized in Figure 20:

The blue lines represent the constraint lines, which in this case are simple supports. The support is simulated by two steel semi-cylinders at the ends of the wing, whose curved contact surface with the wing generates a transverse displacement but allows rotations, as shown in the photo presented in Figure 21:
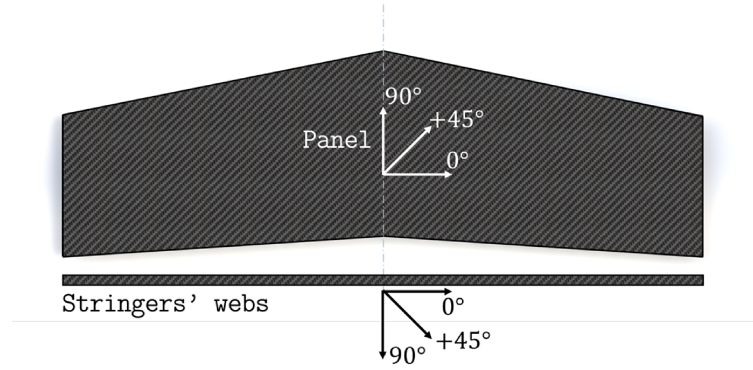
Figure 17: Representation of the fiber orientation in the composite panel
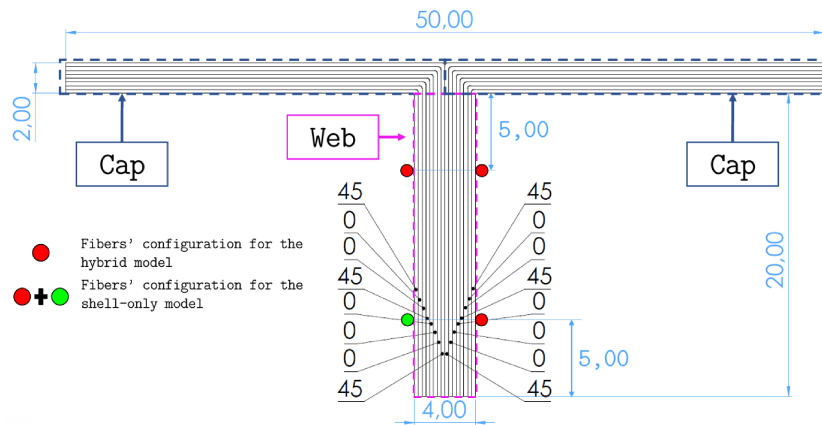
Figure 18: Representation of the section, stacking sequence, and sensor positions on the stringer

$E_{11}[GPa]$	$E_{22}[GPa]$	ν_{12}	$G_{12} = G_{23} = G_{13}[GPa]$	Thickness [mm]
59.7	59.7	0.09	3.8	0.25

Figure 19: Nominal properties of TWILL T-300

As for the application of the load, there were two possibilities, as shown in Figure 20, namely at the two yellow points labeled F1 and F2. The difference between these two cases lies in the fact that at the point corresponding to F1, the force generates a significant torsion of the wing, which does not happen for F2. In this case, the F1 case, with torsion, was chosen.

The load is applied through a steel sphere in contact with the panel, which moves unidirectionally, allowing pressure on the panel via a system of threaded screws. Connected to the threaded screws are the load cells.

The loading system can be seen in Figure 22.

34
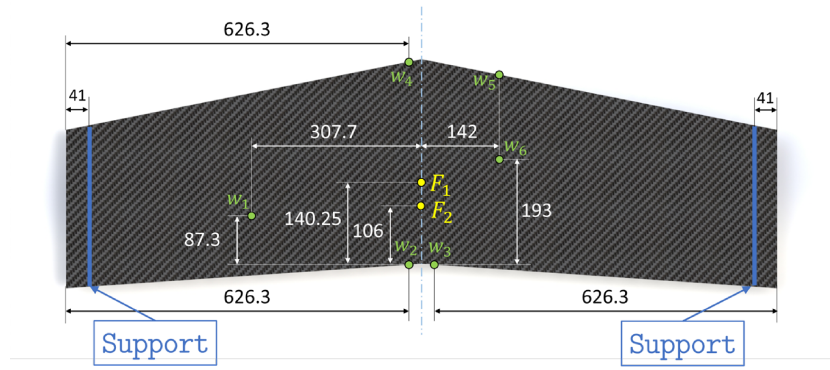
Figure 20: Experimental Setup
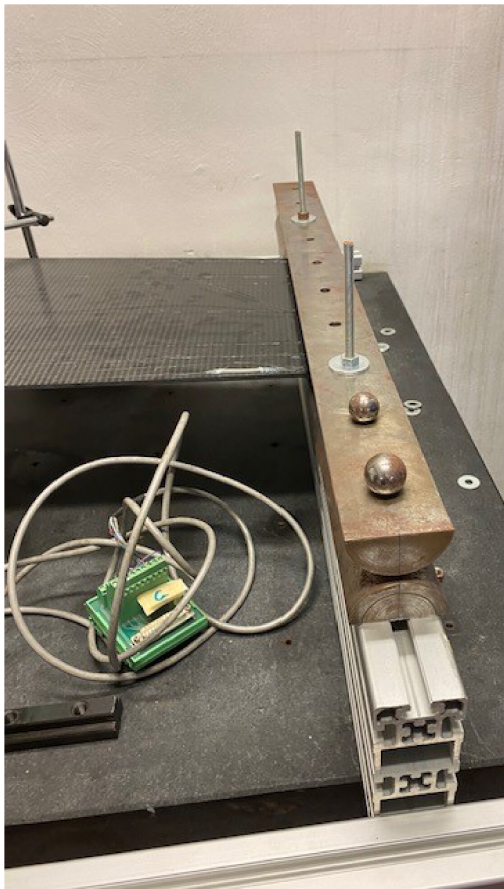
Figure 21: Support
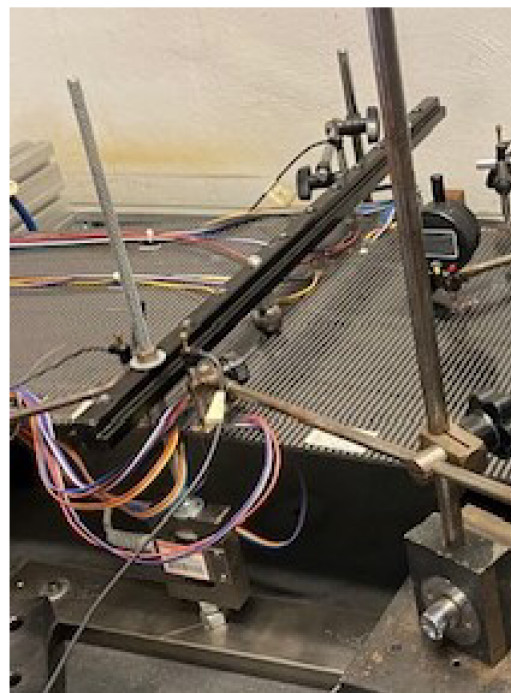
Figure 22: Load System

5.2.2 Strain Sensors

The strains are measured by specific sensors, primarily by an optical fiber sensor. It is based on Optical Frequency Domain Reflectometry (OFDR), which exploits the variation in the characteristics of light within the fiber due to deformation. The fiber is placed on the panel and stringers along the direction from the root of the wing to the tip of the wing. The Optical Fiber is clearly visible in Figure 23:

In addition to the Optical Fiber, there are 16 strain rosettes, which measure

Figure 23: Optical Fiber
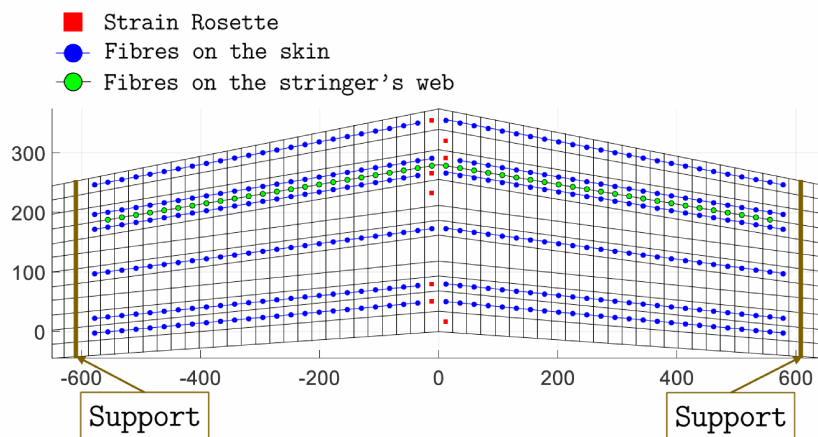
Figure 24: Sensors Position

deformation along 3 axes. They are arranged in such a way that 8 are on the upper surface and 8 on the lower surface, all near the root of the wing.

The arrangement and position of the sensors are shown in Figure 24.

Finally, there are LVDT sensors that measure transverse displacements at specific points. This information is useful because it will later be used as a benchmark to compare with the reconstructed displacements to verify whether the iFEM model is accurate or not.

The position of the 6 LVDT sensors is shown in Figure 25:
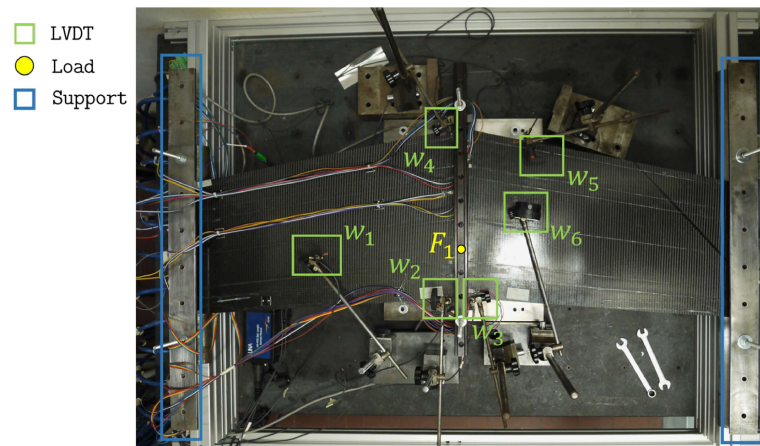
Figure 25: Position of the LVDT Sensors

5.3 iFEM Models

Two iFEM models have been considered, which aim to best represent the actual panel on which the laboratory tests were conducted.

5.3.1 Full iFEM Model

The first is a model that exclusively includes 2-D Shell elements, which thus model both the panel and the stringers, as shown in Figure 26.
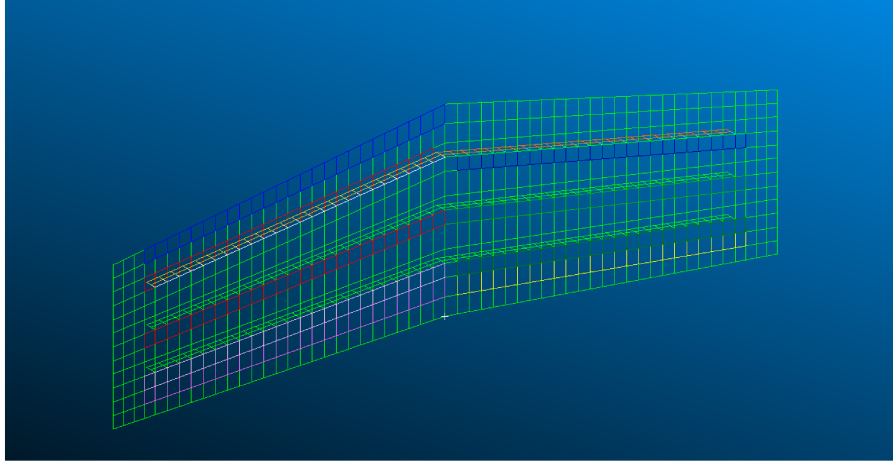
Figure 26: Shell-full panel. The groups of elements representing the areas of the real panel where the optical fiber is present are colored differently.

The position of the sensors on the shell-full panel has been reproduced in the model as shown in Figure 27:
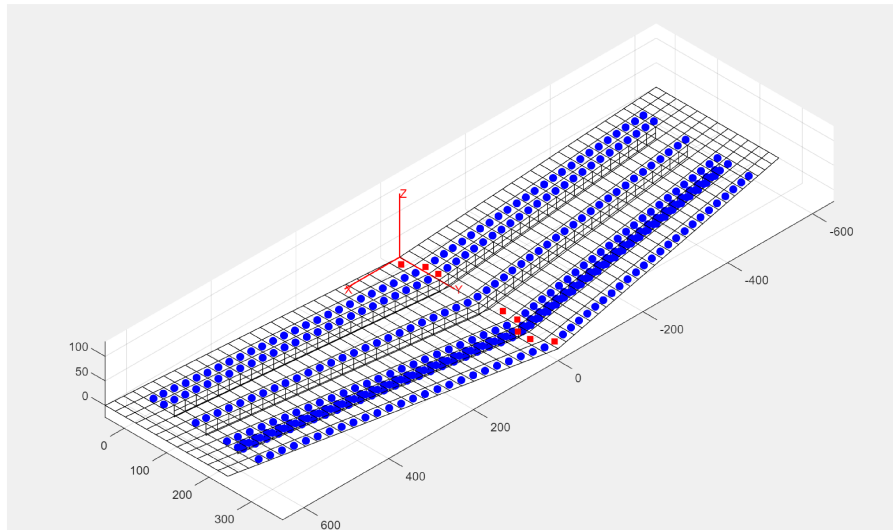
Figure 27: Shell-full model with sensors. The blue points represent the fiber measurement points, and the red points represent the strain rosettes.

The second model is a hybrid model consisting of 2-D shell elements, which model the panel, and 1-D beam elements, which model the stringers, as shown in Figure 28:
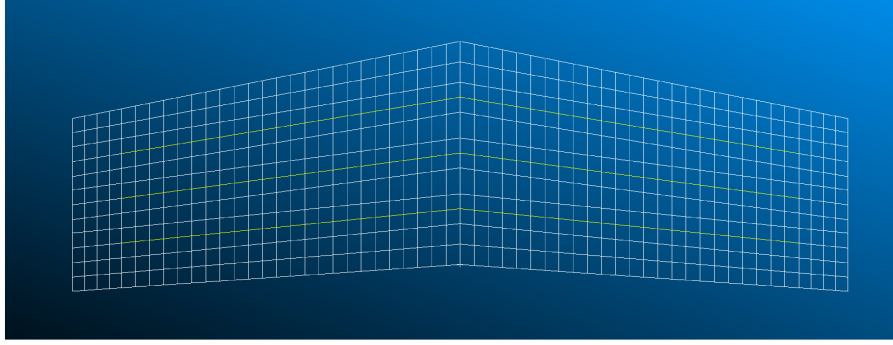
Figure 28: Panel modeled with shell and beam elements. The 1-D elements are colored yellow, as they are a different type of element from the rest of the panel.

The position of the sensors on the shell-beam panel has been reproduced in the model as shown in Figure 29:
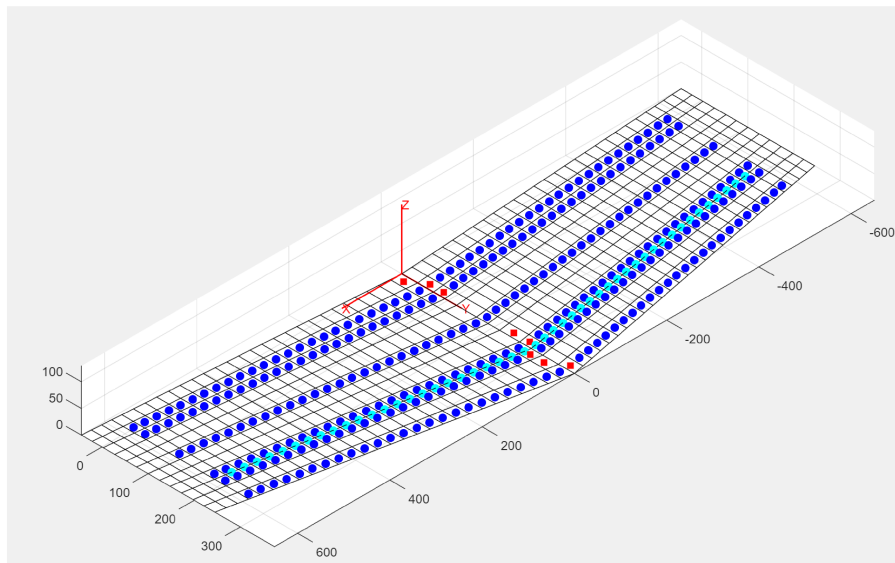
Figure 29: Shell-beam model with sensors. The blue points represent the fiber measurement points, the red points represent the strain rosettes, and the light blue points represent the measurement points on the 1-D elements.

5.3.2 Reduced iFEM Models

Considering the same iFEM models as before, but with a reduced number of sensors, the reduced iFEM models are obtained.

The issue is to verify whether the strains reconstructed using the iFEM method in some unsensed areas of the panel with reduced sensing are accurate, using the measurements from the full models in the same areas as a benchmark.

Figures 30 and 31 show the reduced sensor configurations for the two shell-full and shell-beam models:
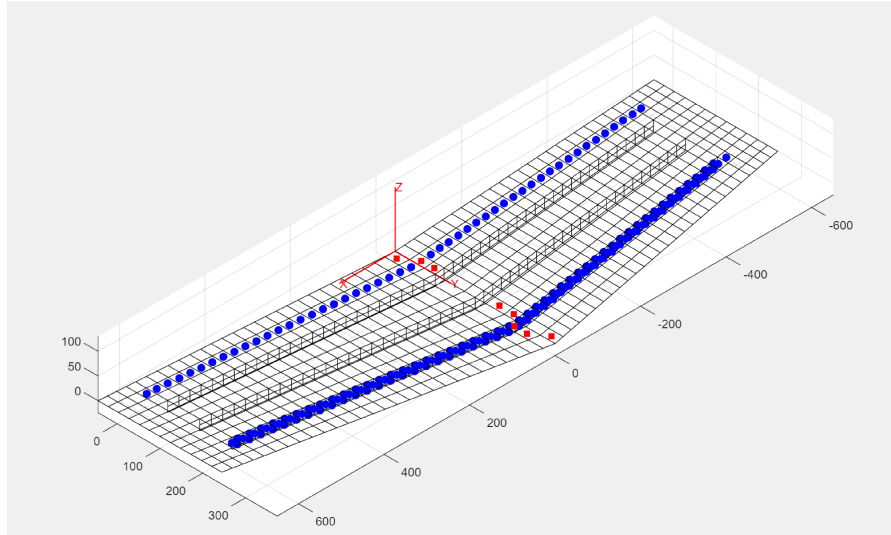
Figure 30: Shell-full model with reduced sensor configuration
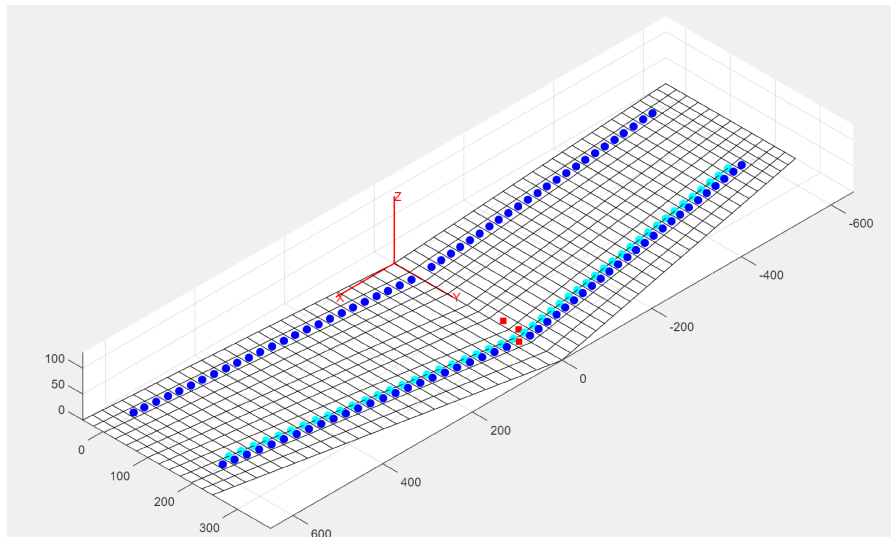
Figure 31: Shell-beam model with reduced sensor configuration

5.4 iFEM Software

The iFEM method has been implemented in the MATLAB executable $"DIMOSS_{G}UI_{v}1"$. This program allows for the reconstruction of the model's nodal degrees of freedom from the strains measured in the laboratory.

Figure 32 shows the initial "Import Data" screen where the inputs for the program are provided:

In the "Import Model" section, the model should be imported, in this case the .bdf file, which can be either shell-full or shell-beam, while in the "Import Plate Strains" section, a file containing the strains measured in the laboratory must be imported.

In the case of the shell-beam hybrid model, in "Import Plate Strains" the strains measured by the sensors on the shell elements should be imported, while in "Import Beam Strains" a file containing the strains measured by the sensors on the
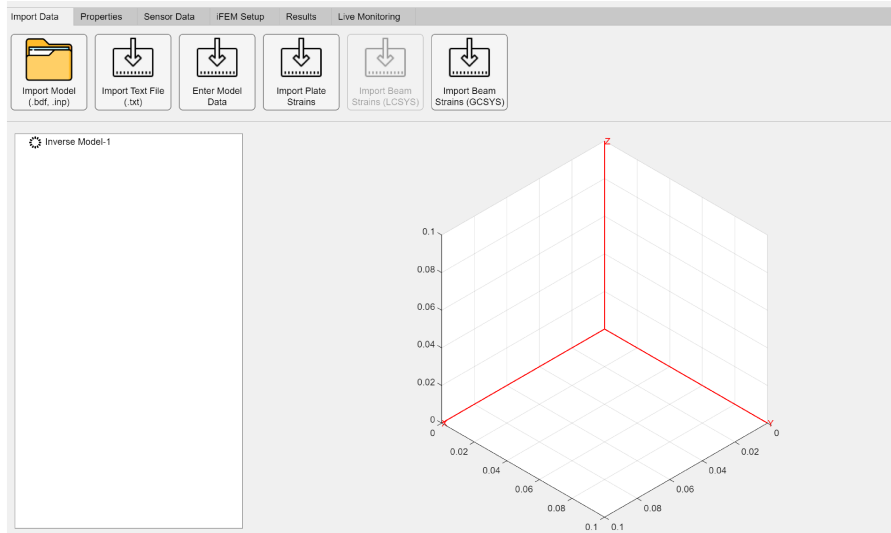
Figure 32: Initial input screen

1-D elements, i.e., the stringers, should be imported. In this latter case, the point on the stringer section where the sensor is attached must also be specified.

The next step, as shown in Figure 33, is to provide the program with the sensorized elements, in this case, uni-directional optical fiber sensors along the x-axis and strain rosettes. In the case of the shell-beam hybrid model, the sensorized 1-D elements must also be provided in the "Beams" section.
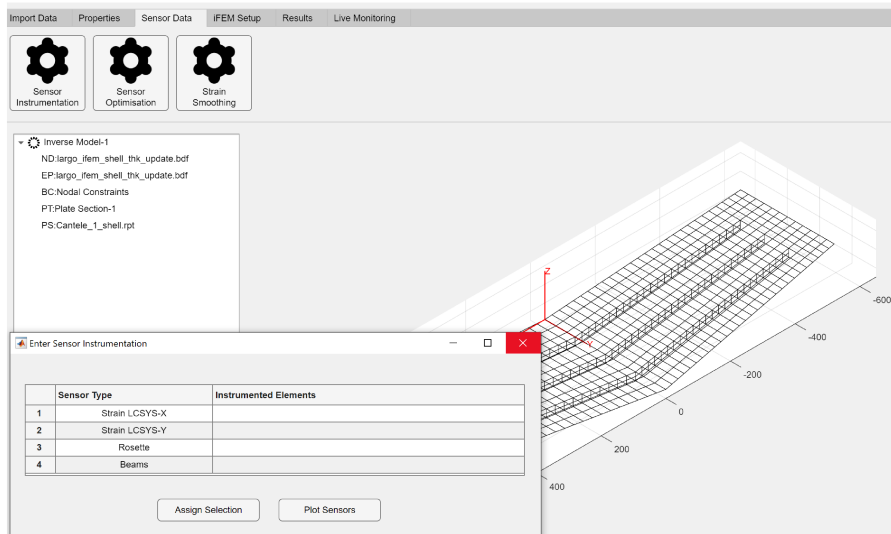

Figure 33: Sensor input screen

At this point, given the experimental strains, the iFEM model, and the sensor positions, it is possible to reconstruct the nodal degrees of freedom, i.e., displacements and rotations.

Then, it is possible to use these nodal degrees of freedom as input to calculate the strains using the method previously outlined and then compare them with the
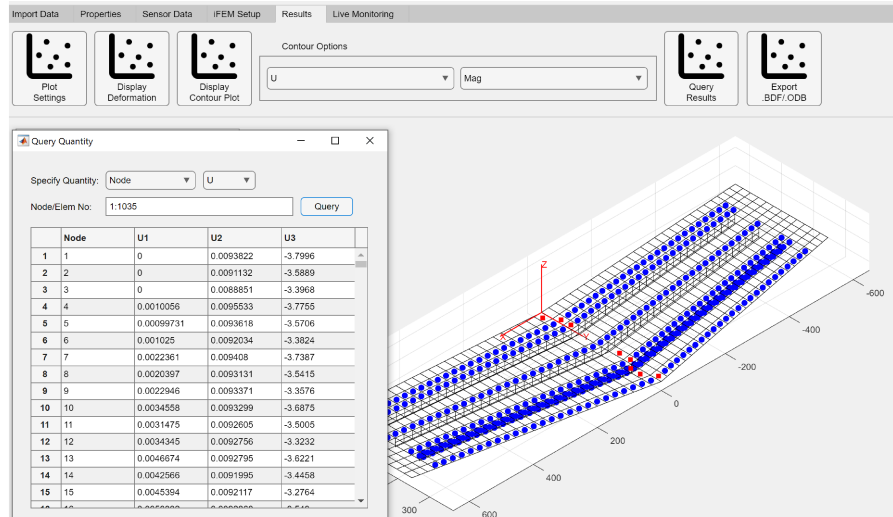
41

Figure 34: Screen showing the nodal degrees of freedom (program output)

experimental strains.

5.5 Results

To summarize, the iFEM program outputs nodal displacements and rotations, which in turn become input for the MATLAB code that implements the strain calculation method previously described.

It is therefore necessary to analyze the results obtained from the various models, check if the errors are contained, and if the strains reconstructed in the reduced models are indeed similar to those measured in the full-sensorized models.

5.5.1 Reconstruction of displacements and rotations

As an initial check of the effectiveness of the iFEM code, it is necessary to see if the reconstructed displacements are consistent with the measured ones. The displacements are reconstructed by the iFEM code from the measured strains, and they should therefore be compared with the ones measured by the LVDT sensors. To verify the agreement of the degrees of freedom, five nodes were selected: node 114, 6, 426, 635, and 302, as shown in Table 1:

Where the displacement being measured and compared is the transverse displacement.

The comparison is made for all four models, both beam and shell, both full and reduced. It is observed that the shell models reconstruct certain degrees of freedom in some elements better, while the beam models are more accurate for other elements.

On average, the full models remain the most accurate, but having a reduced sensor configuration is beneficial in terms of optimizing the instrumentation.

For some elements, the percentage errors in the displacement reconstruction are very small, ranging from 0 to 3%, while for other elements, the errors increase.

However, it should be noted that element 426, which presents errors between 5%

Experimental	-2,58	-3,21	-3,14	-4,93	-5,42
iFEM (shell) ijk	-2,67	-3,38	-3,38	-4,68	-5,23
Error (%)	3,50	5,24	7,71	-5,19	3,50
iFEM (shell reduced) ijk	-2,62	-3,46	-3,46	-4,33	-4,71
Error (%)	1,43	7,61	10,13	-12,20	-13,03
iFEM (beam) ijk	-2,69	-3,38	-3,38	-4,81	-5,38
Error (%)	4,17	5,17	7,63	-2,55	-0,64
iFEM (beam reduced) ijk	-2,65	-3,44	-3,44	-4,79	-5,29
Error (%)	2,93	7,05	9,57	-2,99	-2,34

Table 1: Table of experimental data and iFEM results

and 10%, is an element of the panel near the stringer, so there is a combination of displacements between two components of the structure. On the other hand, elements 635 and 302 are near the support area, so the displacements are influenced by the presence of the constraint, and a higher error is expected.

These small errors in the reduced models are an initial indication of how the iFEM method generally reconstructs the degrees of freedom well and, as will be shown, the strains in the uninstrumented points.

5.5.2 Fibers

Before analyzing the results, it is necessary to unambiguously define the parts of the panel instrumented with optical fiber. The following Figures 37 and 38 show these parts:
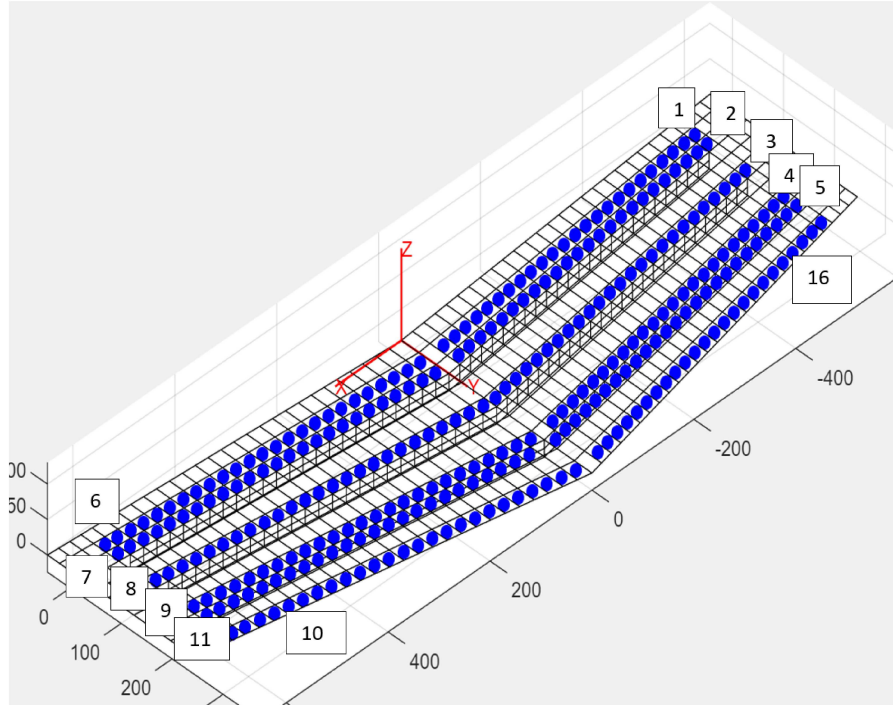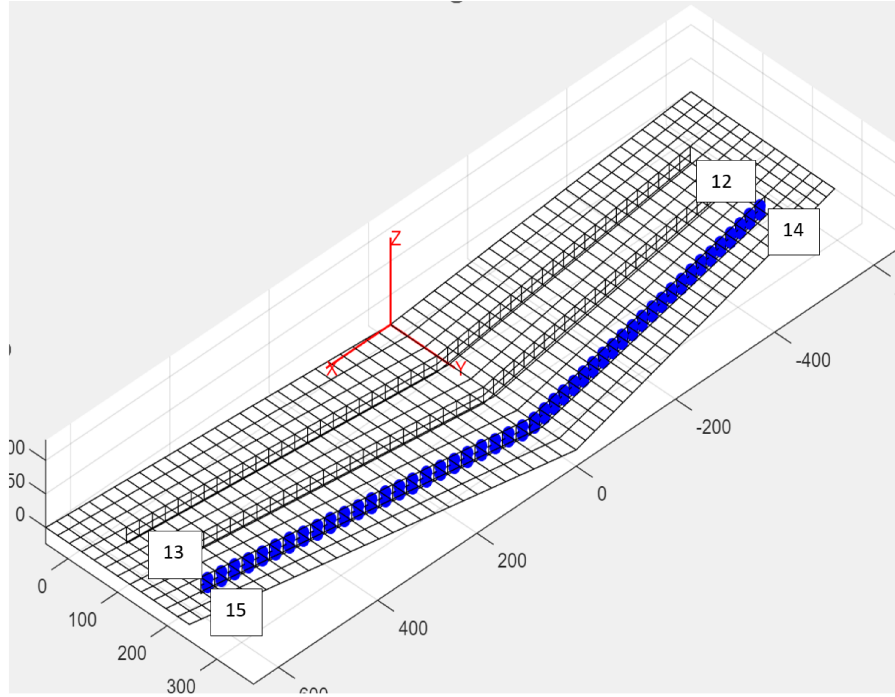

Figure 35: Sensorized parts (Fibers)

Figure 36: Sensorized parts (Fibers)

highlighting the groups of model elements corresponding to sensorized parts (Fibers) with their corresponding numbers. In the first figure, the elements are on the panel, in the second on the stringers.

5.5.3 Results for the Shell Full Model

The shell full model exclusively contains 2-D shell elements and is sensorized in such a way that it accurately represents the real panel.

Analyzing Figure 37, the sensorized part called "Fiber 1,"
where on the x-axis are the elements that make up a specific fiber, and on the y-axis is plotted the micro-strain along the x-axis. It is evident that the two curves almost overlap, but it is necessary to analyze the relative error, calculated as follows:

$$error = \left| \frac{(\epsilon_c - \epsilon_m)}{\epsilon_m} \right| \tag{129}$$

where ϵ_c are the calculated strains and ϵ_m are the measured strains.
The error trend for Fiber 1 is shown in Figure 38, where it can be seen that the error stays below 0.65%, demonstrating the excellent accuracy achieved.

Analyzing, for example, Fiber 3, as seen in Figure 39:
It can also be noted in this case the remarkable accuracy with which the iFEM method approximates reality, although in this case, as seen in Figure 40, the errors are around 1%.
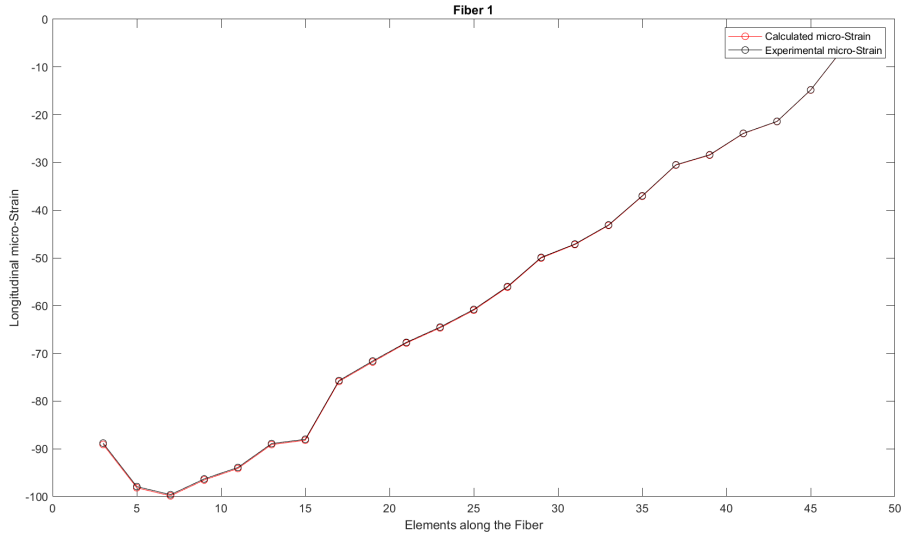
44

Figure 37: Micro-Strain along Fiber 1. The red dots represent the strains calculated using the iFEM method, and the black dots represent the experimentally measured strains.
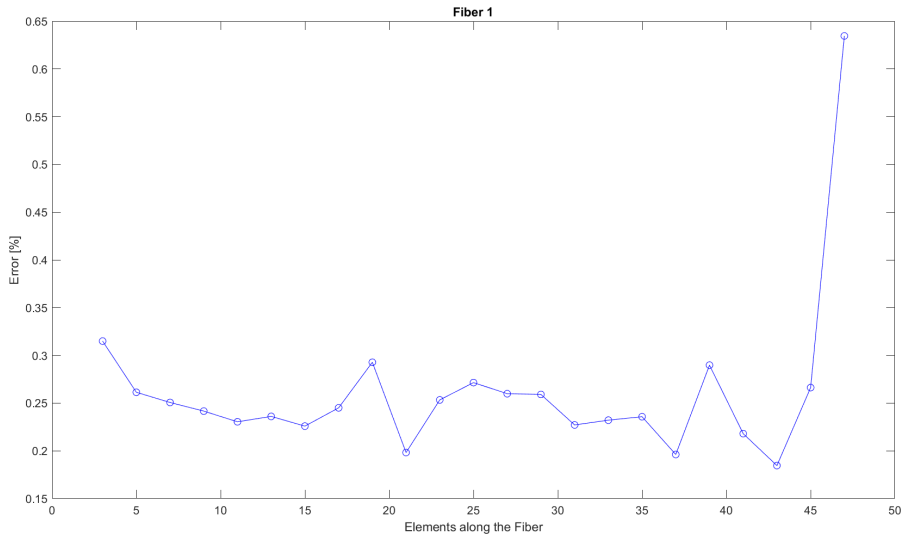

Figure 38: Error along Fiber 1

Now, in Figures 41, 42, 43, and 44, strain values and relative error are shown for a line of elements corresponding to "Fiber 12" and "Fiber 13", that is, 2-D shell elements modeling the stringers, thus presenting different planes compared to the panel:

There is a good overlap of the strain plots, although they are generally less accurate compared to the elements of the panel. In fact, the error ranges from 0.5% to 1%, but it reaches peaks over 2% for "Fiber 12" and 3% for "Fiber 13". From this data, two possibilities can be deduced. The first possibility is that the strain measurement is less precise when taken along the stringer, but there is no evidence of this. The second, more probable possibility is that the iFEM method reconstructs the displacements and rotations of the stringers with greater difficulty, as these components have a specific section and plane different from that of the
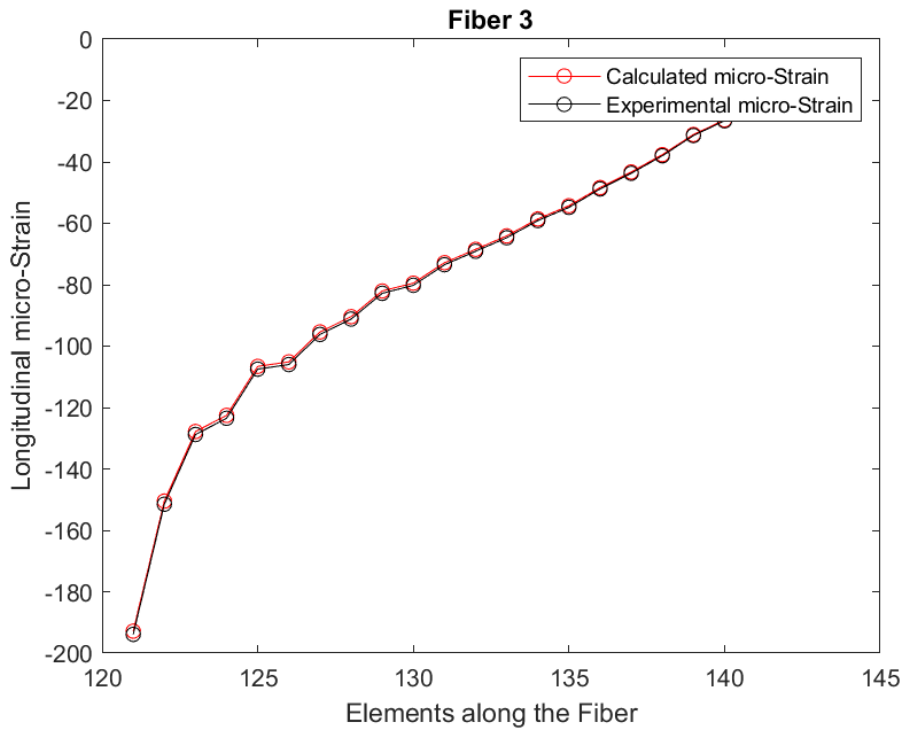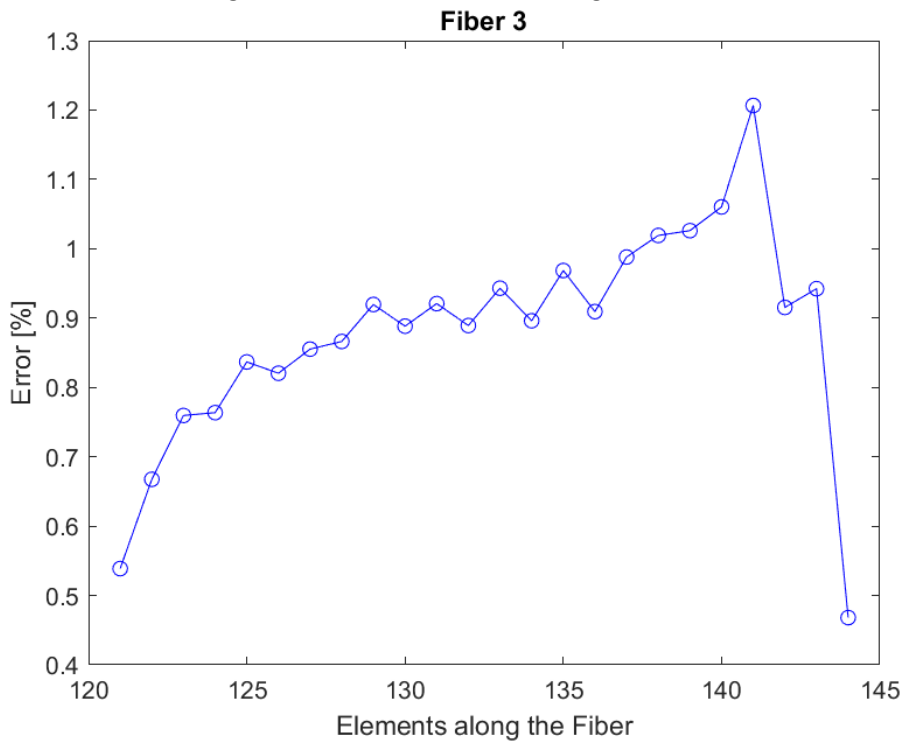
45

Figure 39: Micro-Strain along Fiber 3

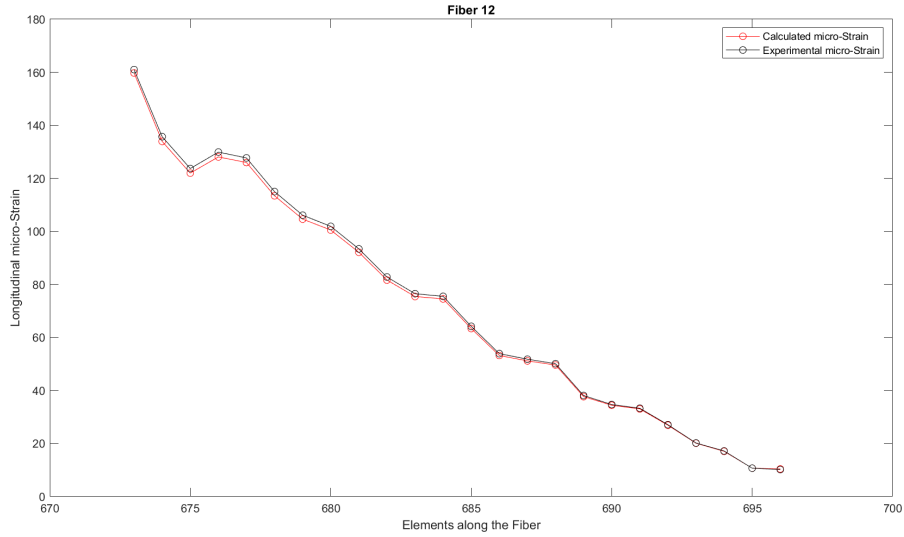Figure 40: Error along Fiber 3
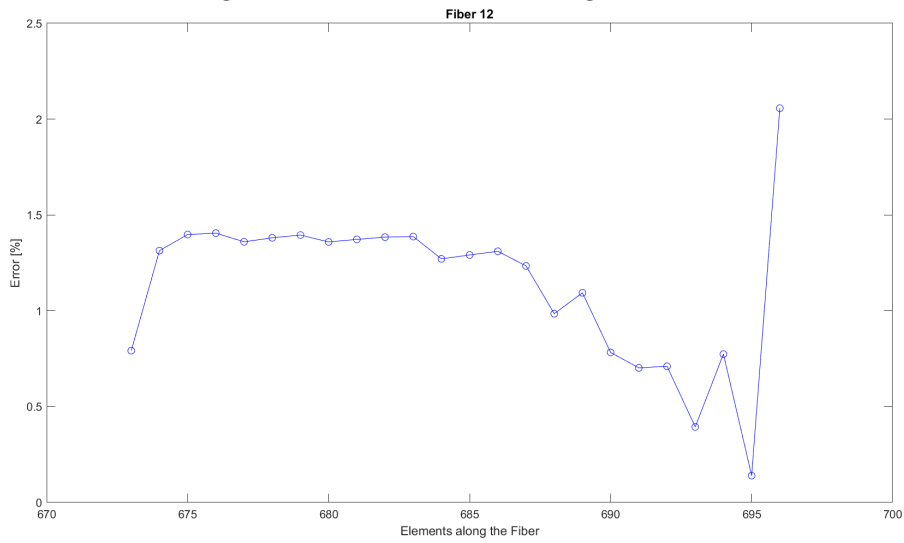
panel.

Figure 41: Micro-Strain along Fiber 12

Figure 42: Error along Fiber 12

5.5.4 Results for the Shell Reduced Model

The goal now is to check whether the shell reduced model, that is, the shell model with fewer sensors than the original, is able to reconstruct the strains in areas that are only sensorized in the shell-full model.

It is important to highlight an aspect that will be fundamental also in the beam reduced model, namely that the iFEM method is a method that takes the experimentally measured strains as input and uses the least squares method for approximation. As a result, the more data provided as input, the greater the calculation precision. It is necessary to verify whether the reconstructed strains in the unsensorized areas in the reduced models are accurate or not, by comparing them with the measured strains.

The strains and the relative error for Fiber 2 are shown in Figures 45 and 46,

It is clearly noticeable that the reconstructed strains closely follow the trend of the experimental ones, although the errors are slightly higher compared to the
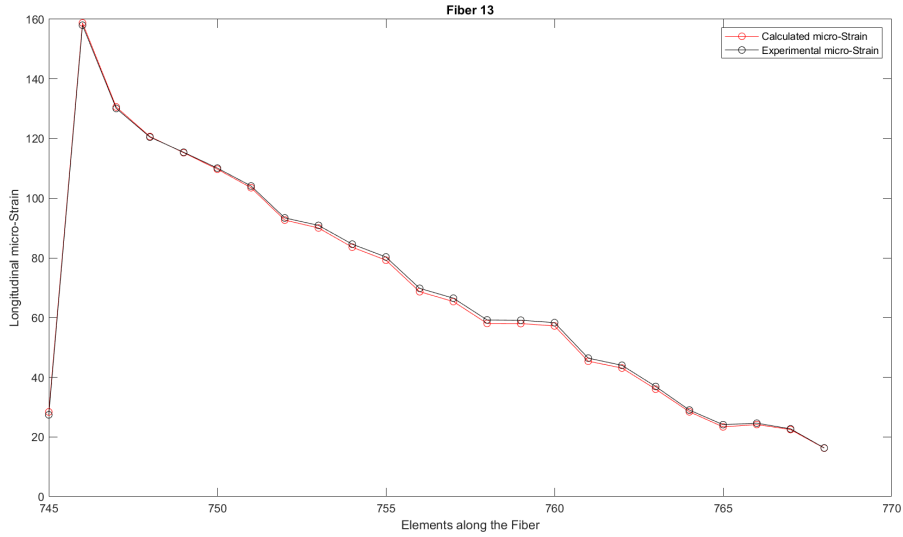
47

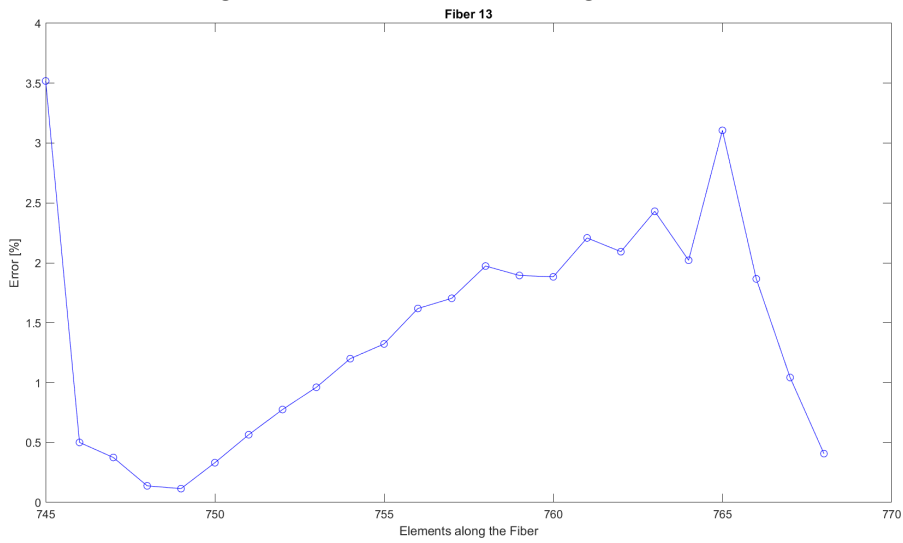Figure 43: Micro-Strain along Fiber 13

Figure 44: Error along Fiber 13

shell-full case.

From the error graph, it can be seen that the errors tend to remain below 5-6%, except for some out-of-range values. However, the error trend increases as we move towards the outer part of the wing, and for the final element (n.72), the error is high, as shown in the strain graph, reaching values over 90%. This can be explained by the fact that as the strains move towards the wing tip, they decrease, eventually approaching very small values close to 0. Consequently, it is difficult to accurately reconstruct the exact strain values, and moreover, the error is not a critical factor for the structural integrity.

Considering, for example, Fiber 9, whose micro-strains and error are plotted in Figures 47 and 48, it can be observed that the calculated strain curve follows the trend of the experimental ones, with a certain degree of error.

It is evident that for some elements, errors reach peaks of 70%. However, this can be explained by the fact that the strain difference is related to a value of 16
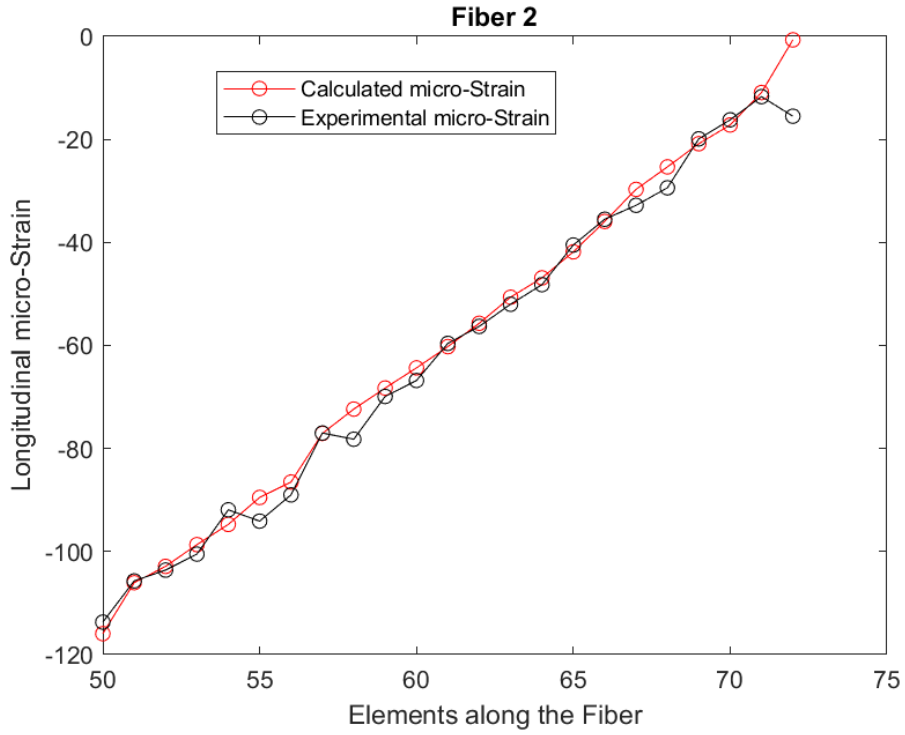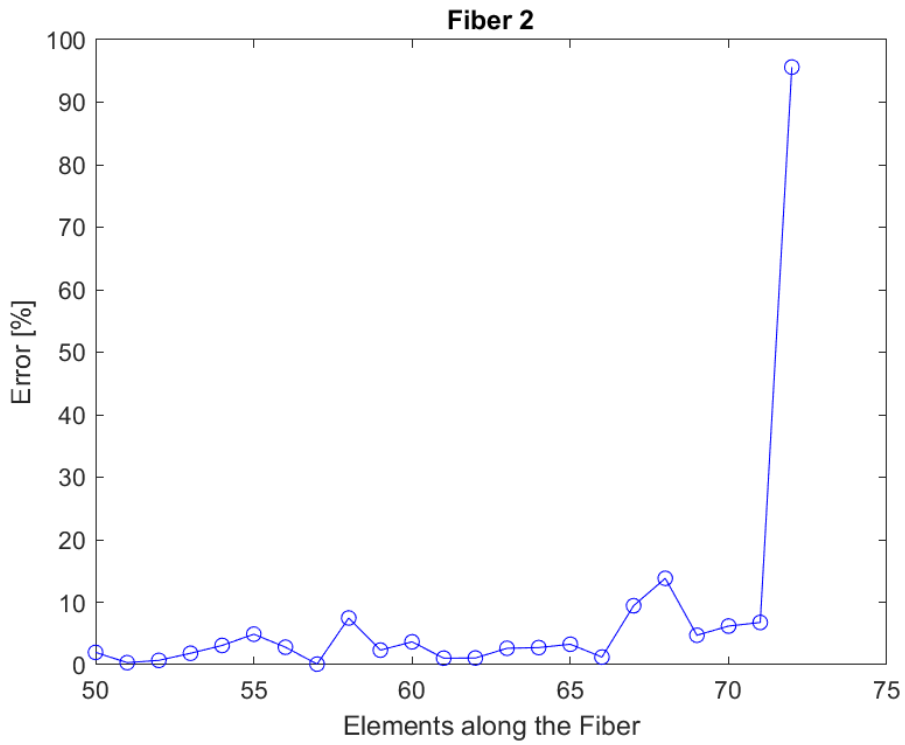
Figure 45: Micro-Strain along Fiber 2

Figure 46: Error along Fiber 2

micro-strain, which is a very small value, close to zero, so it is understandable that the relative errors increase.

It can be seen that for element 529, the error is around 40%, while the error curve remains stable at values below 10% for the adjacent elements. The difference in
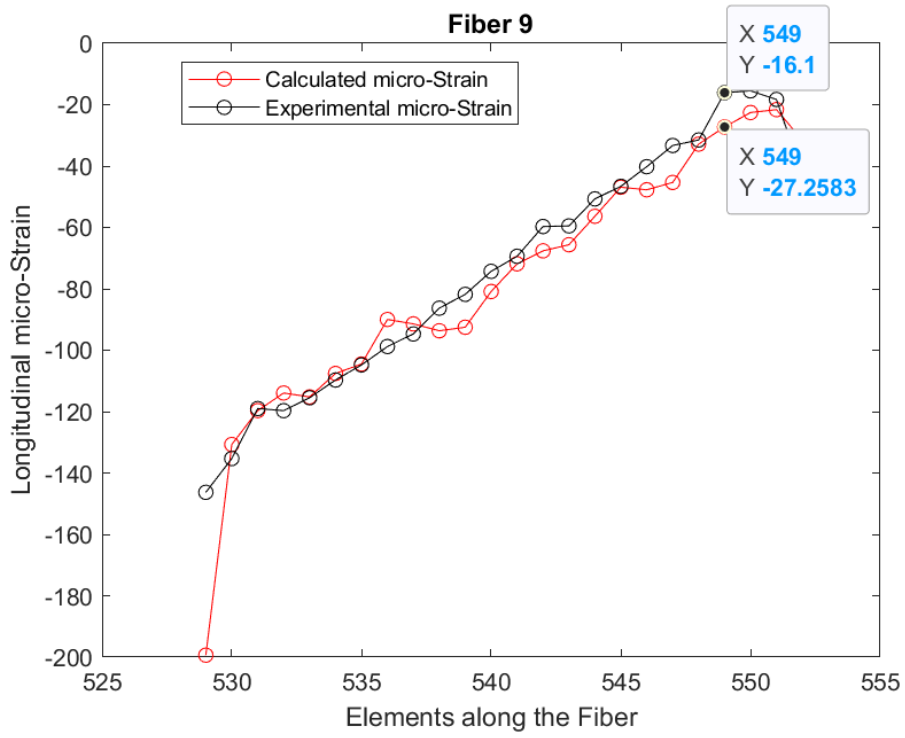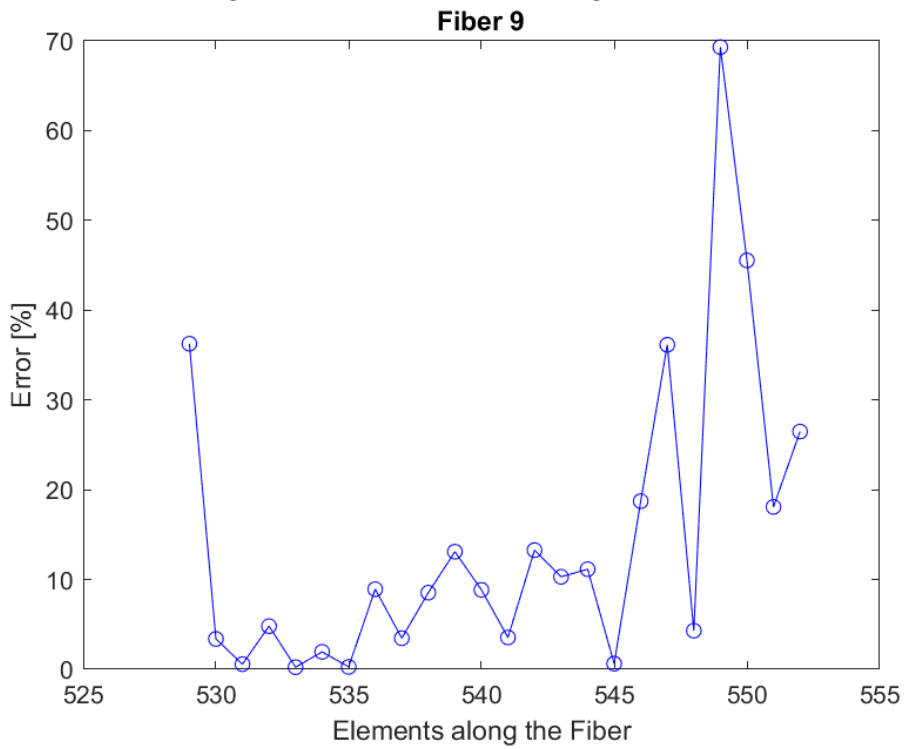
Figure 47: Micro-Strain along Fiber 9

Figure 48: Error along Fiber 9

the strain behavior is due to local effects, but globally, the reconstructed trend matches the measured one.

5.5.5 Beam Full Model Results

The beam full model has fewer elements compared to the shell full model, as the stringers are modeled with 1-D elements. Consequently, the number of sensors to be inserted into the iFEM software for the beam full model is smaller than the number of sensors required for the shell full model, and therefore, the accuracy with which strains are calculated varies.

For example, by analyzing Fiber 4 and Fiber 10 as shown in Figures 49, 50, 51, and 52:

It is immediately noticeable that the calculated strain curves closely follow the measured strain curves, with errors below 1%.

This result implies that the slightly lower number of sensors does not affect the accuracy of the strain calculation, as the sensor lines are the same as those in the shell full model, except for the stringers. It can therefore be concluded that whether choosing the shell full or beam full model, the differences in strain calculation on the panel are minimal.

This is an important result, as it implies that a hybrid 1-D and 2-D model is almost equivalent, in terms of calculation accuracy, to a 2-D model, despite the computational advantages and greater simplicity.

5.5.6 Beam Reduced Model Results

The beam reduced model has a significantly smaller number of sensors compared to the shell full model, both because the number of elements in the beam model is fewer than in the shell model due to the presence of 1-D elements, and because the sensor configuration is reduced. Therefore, the number of input measurements is the minimum among the four configurations, and lower accuracy is expected in reconstructing strains at the unsensed points.

Figures 53 and 54 below show the micro-strain and error in Fiber 2, the same one considered in the shell reduced model, allowing for a comparison:

It is immediately noticeable that the trend of the calculated micro-strain closely follows the measured one, but to better understand the difference with the one obtained in the shell reduced model, it is useful to observe the error.

The error trend is very similar to that of the shell reduced model. It remains within values below 10% for a long portion of the Fiber, then increases towards the end, reaching peaks of around 70%. This trend has already been explained in the chapter related to the shell reduced model, but it is now more interesting to compare the magnitude of the errors.

It can be seen that in the first part, the errors are within the 0-10% range, but in the case of the beam reduced model, the curve is less flat and contains more peaks, reaching around 10%.

The average error in this part of the graph is therefore higher in the beam reduced model case, but this is justifiable by the lower accuracy due to the approximation of the stringers with 1-D elements and the corresponding difference in sensors. The differences in the error are still limited, and the results are excellent.

It is also important to note that at element 72, the error is around 70%, while in the shell reduced case it is around 100%. It can be deduced that representing the
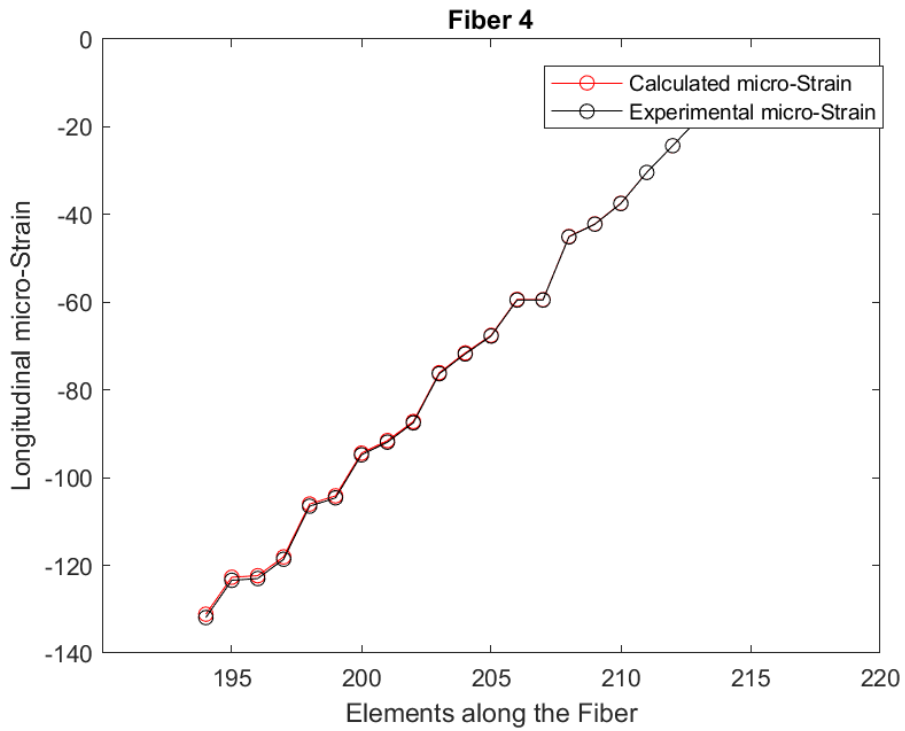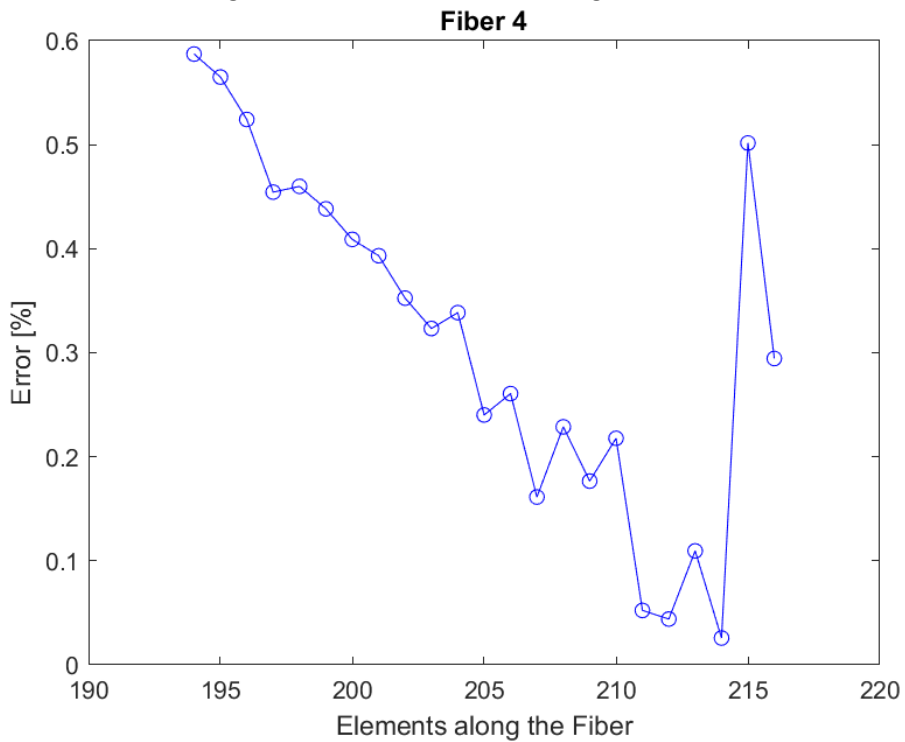
Figure 49: Micro-Strain along Fiber 4

Figure 50: Error along Fiber 4

stringers as 1-D elements was more effective in capturing the edge effects, as the stringer ends at that point.

Now, observing Fiber 16, as shown in Figures 55 and 56:

It can be observed, as highlighted, that there is a portion of the Fiber where

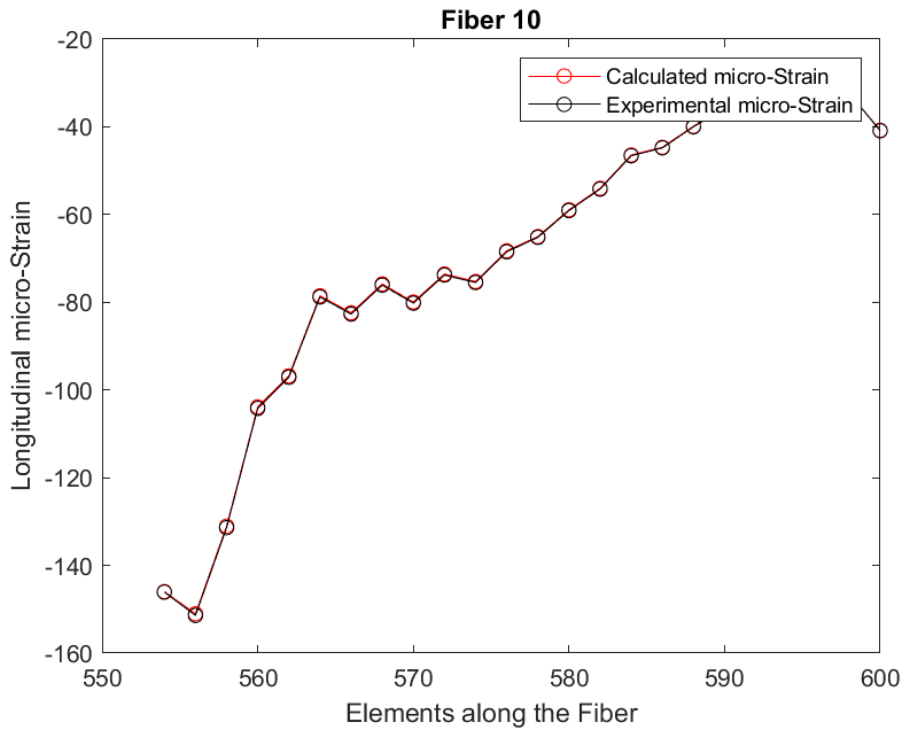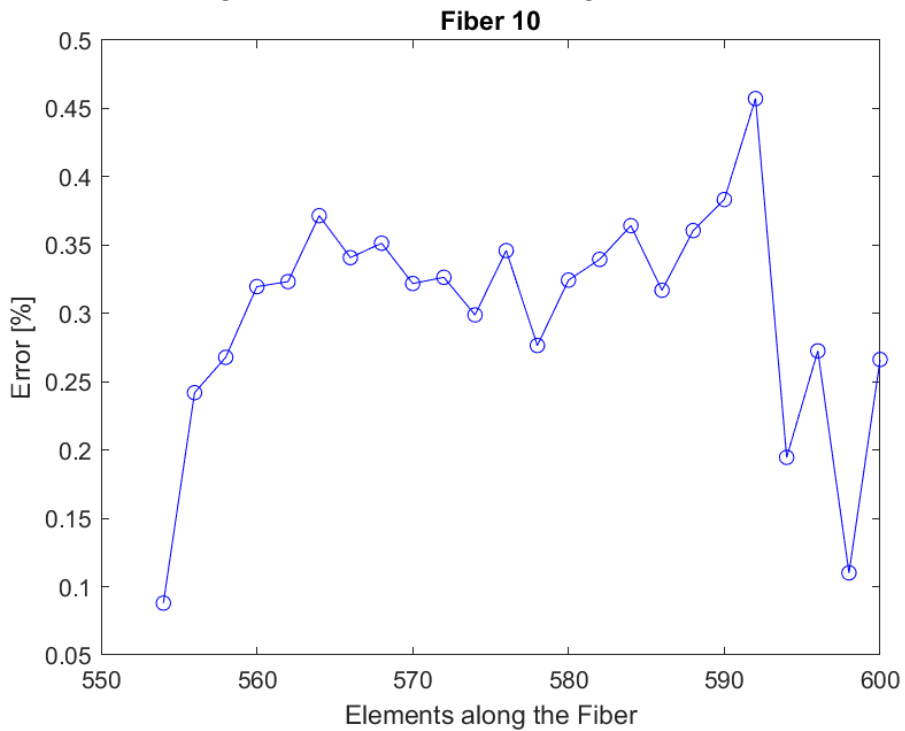Figure 51: Micro-Strain along Fiber 10

Figure 52: Error along Fiber 10

the error curve is flat and remains around 10%, so the approximation is excellent. As in the previous cases, the error increases as we move to the right on the graph, but it can be observed that the micro-strain approximation is still respected. The explanation is therefore the same as previously mentioned in other cases: first,

53

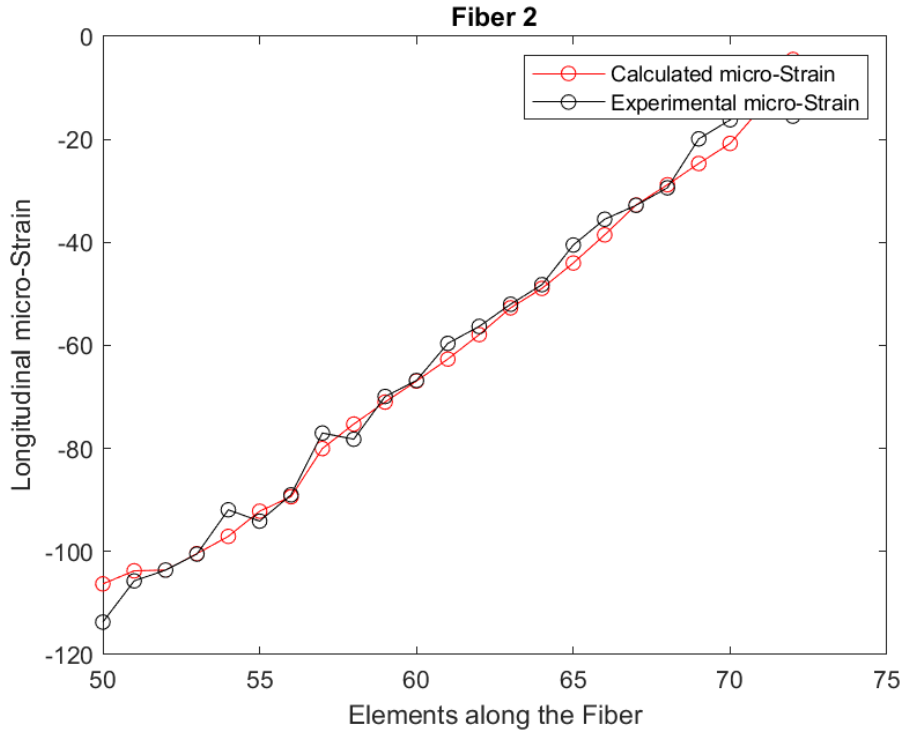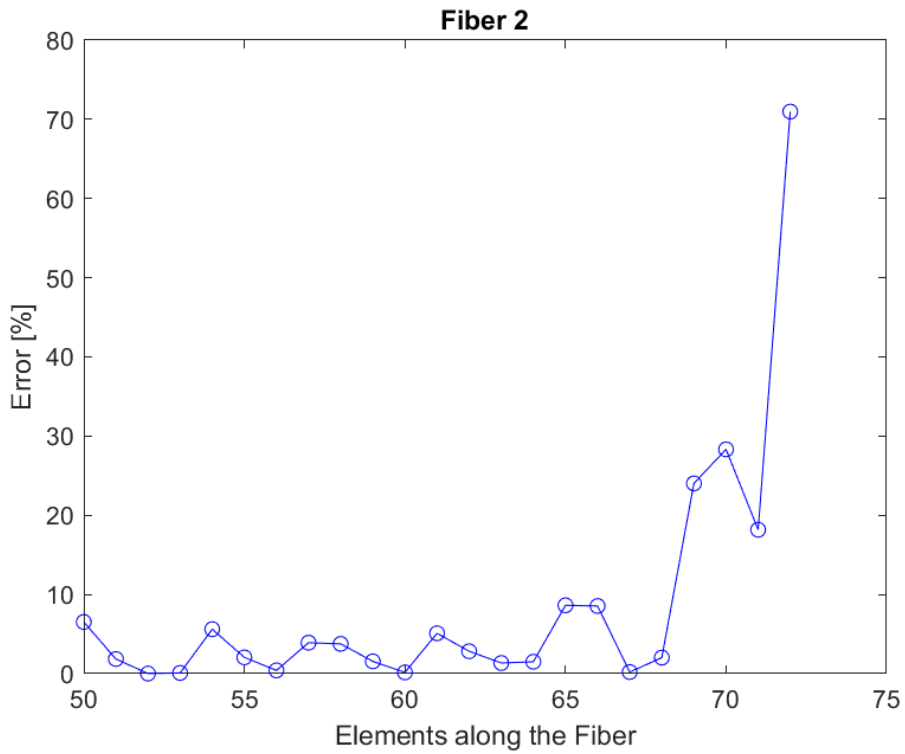Figure 53: Micro-Strain along Fiber 2

Figure 54: Error along Fiber 2

element 264, where the error is very high (250%), is an element close to the support, and second, it involves very small micro-strain values, close to zero, which makes the relative error large. Indeed, the error values are slightly above and below zero.
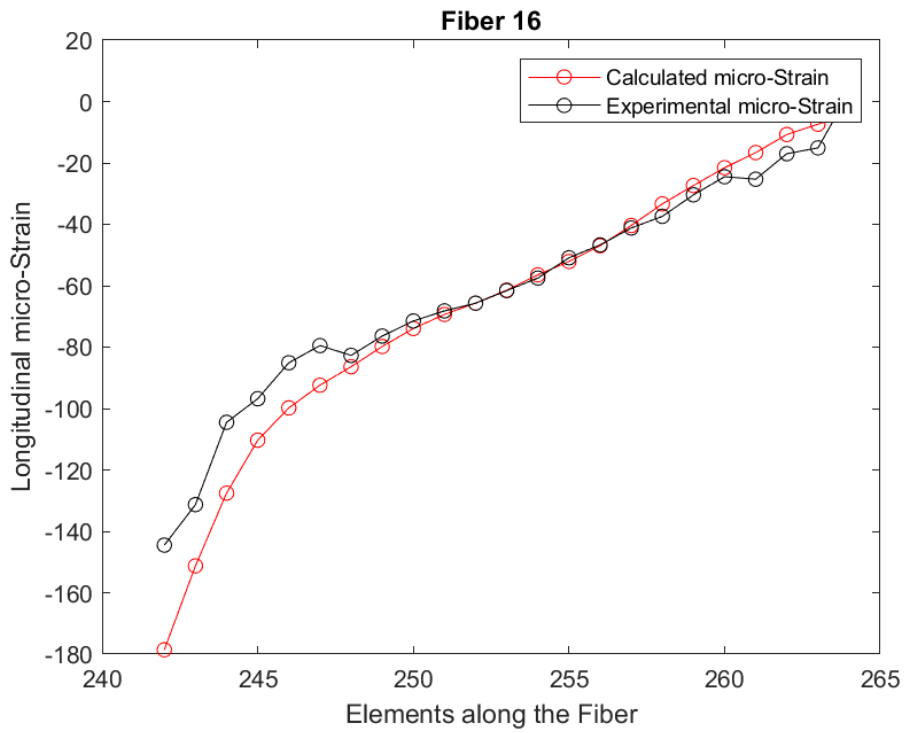
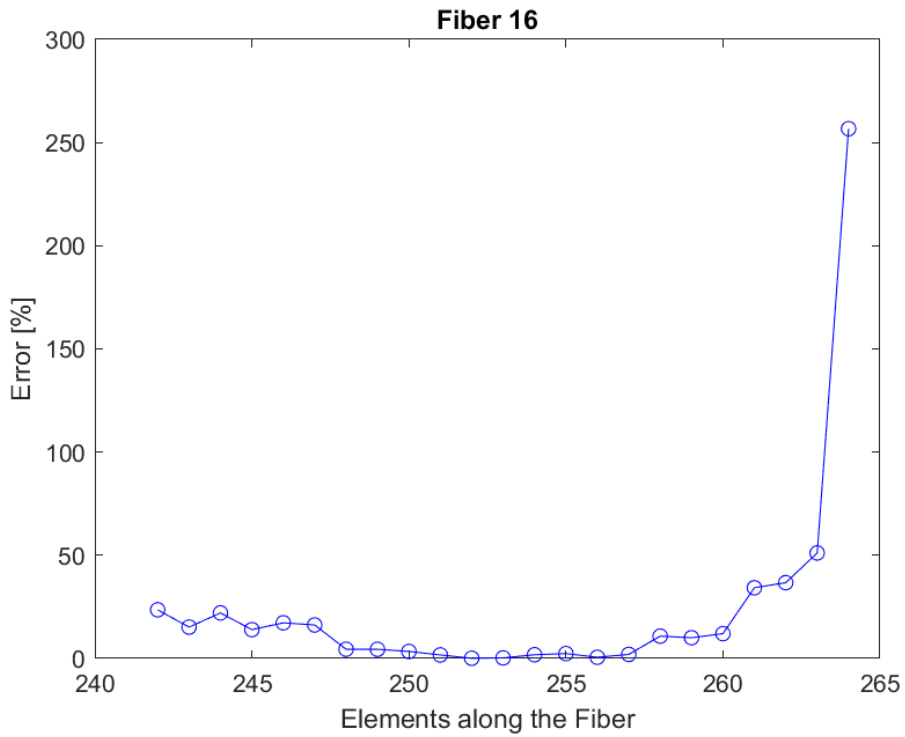Figure 55: Micro-Strain along Fiber 16

Figure 56: Error along Fiber 16

6 Conclusions

The iFEM method is a structural analysis method for shape-sensing that, starting from an iFEM model of a structure and a certain number of experimentally measured strains of the same structure, reconstructs the degrees of freedom of the structure, i.e., displacements and rotations. This operation is mathematically carried out by minimizing an error function that takes into account the difference between the analytical and experimental deformations. From the nodal degrees of freedom of the model, it is possible to reconstruct the deformations in each element. To verify the effectiveness of the method, measured and calculated deformations can be compared.

An experimental test was carried out on a structure, which in this case is a composite wing-shaped panel, supported at the ends with a load applied at midspan. The deformations were measured along specific measurement lines using an optical fiber sensor and at specific points using strain gauges.

Furthermore, displacements were measured using LVDT sensors at specific points. These measured displacements were compared with those reconstructed by the iFEM code, and a good agreement was observed between the two, with errors typically in the range of a few percentage points.

To verify the accuracy of the procedure for calculating deformations from nodal displacements, a simplified panel model was analyzed using MSC.Patran and Abaqus FEA software, where it was found that the deformations at the centroids of the elements indeed correspond to those calculated from the nodal degrees of freedom calculated by Abaqus FEA.

Two models of the actual panel were created: one entirely made up of 2-D shell elements (shell model) and one hybrid with 1-D beam elements (beam model). For both cases, two configurations were analyzed: one where the number and position of the sensors are faithful to the real component (full configuration) and one where the number of sensorized elements is smaller (reduced configuration).

Thus, the real panel model was analyzed, and it was observed that the deformations calculated at the centroids of the elements corresponding to the sensorized parts of the structure are very similar to the experimentally measured ones. The errors in this case are generally below 5%, both for the shell model and the beam model. Therefore, it can be concluded that approximating the stringers with 1-D beam elements and having fewer sensors on the stringers compared to the shell case do not significantly affect computational accuracy.

In the reduced configurations, it was found that the reconstruction of deformations on the panel is accurate, with errors similar to the full configuration, while the reconstruction of deformations in the unsensed elements produces larger errors. This is due to the fact that the number of experimentally measured deformations provided as input to the iFEM code is lower, which influences the least squares approximation method.

In general, relative errors increase where the deformation values are infinitesimal, but this fact is justifiable and of little relevance, as deformations close to zero are difficult to reconstruct perfectly and do not pose a threat to the structural integrity. As a future development, it will be possible to calculate stresses from the reconstructed strains. To do this, it will be necessary to know the material properties

of the elements, especially the stiffness matrix.

Knowing the stresses is important for assessing the state of the structure in real-time (Structural Health Monitoring).

Regarding the iFEM method in general, the most interesting future prospects involve its application to complex structures, including spatial ones. The increasing complexity of structures implies that non-linear iFEM methods will need to be refined.

For example, fuselages and wings are subjected to high pressure loads during flight, which produce significant deformations. An iFEM method that reconstructs the deformed shape from a set of measured deformations would be useful for monitoring potential buckling failures.

Other structures that experience significant deformations include solar sails, de-orbiters, and sunshields (such as the one on the James Webb Space Telescope). Again, monitoring through shape sensing is an interesting prospect in these cases.

7 Bibligrafia

[1]. Tessler, A.; Spangler, J.L. "A Variational Principle for Reconstruction of Elastic Deformations in Shear Deformable Plates and Shells" NASA/TM-2003-212445 2003

[2]. Tessler, A.; Spangler, J.L. "A least-squares variational method for full-field reconstruction of elastic deformations in shear-deformable plates and shells" Computer Methods in Applied Mechanics and Engineering 2005

[3]. Tessler, A.; Spangler, J. "Inverse FEM for Full-Field Reconstruction of Elastic Deformations in Shear Deformable Plates and Shells" Proceedings of Second European Workshop on Structural Health Monitoring 2004

[4]. Mindlin, R. "Influence of rotatory inertia and shear on flexural motions of isotropic, elastic plates" J. Appl. Mech. 1951

[5]. Kefal, A.; Oterkus, E.; Tessler, A.; Spangler, J.L. "A quadrilateral inverse-shell element with drilling degrees of freedom for shape sensing and structural health monitoring" Engineering Science and Technology, an International Journal 2016

[6]. Kefal, A. "An efficient curved inverse-shell element for shape sensing and structural health monitoring of cylindrical marine structures" Ocean Engineering 2019

[7]. Gherlone, M.; Cerracchio, P.; Mattone, M.; Di Sciuva, M.; Tessler, A. "Shape sensing of 3D frame structures using an inverse Finite Element Method" International Journal of Solids and Structures 2012

[8]. Farrar, C.R.; Worden, K. "An Introduction to Structural Health Monitoring" Philosophical Transactions of the Royal Society A: Mathematical, Physical and Engineering Sciences 2007

[9]. Heaney, P.S.; Ivanco, T.G.; Bilgen, O. "Distributed sensing of a cantilever beam and plate using a fiber optic sensing system" Applied Aerodynamics Conference 2018

[10]. Kefal, A.; Tessler, A.; Oterkus, E. "An enhanced inverse finite element method for displacement and stress monitoring of multilayered composite and sandwich structures" Composite Structures 2017

[11]. Esposito, M.; Gherlone, M. "Material and strain sensing uncertainties quantification for the shape sensing of a composite wing box" Mechanical Systems and Signal Processing 2021

[12]. Oboe, D.; Colombo, L.; Sbarufatti, C.; Giglio, M. "Shape Sensing of a Complex Aeronautical Structure with Inverse Finite Element Method" Sensors 2021

[13]. Tessler, A.; Roy, R.; Esposito, M.; Surace, C.; Gherlone, M. "Shape Sensing of Plate and Shell Structures Undergoing Large Displacements Using the Inverse Finite Element Method" Shock and Vibration 2018

[14]. Abdollahzadeh, M.; Ali, H.; Yildiz, M.; Kefal, A. "Experimental and numerical investigation on large deformation reconstruction of thin laminated composite structures using inverse finite element method" Thin-Walled Structures 2022

[15]. Roy, R.; Gherlone, M.; Surace, C. "A shape sensing methodology for beams with generic cross-sections: Application to airfoil beams" Aer. Sci. and Tech. 2021

[16]. Zhao, F.; Xu, L.; Bao, H.; Du, J. "Shape sensing of variable cross-section beam using the inverse finite element method and isogeometric analysis" Measurement: Journal of the International Measurement Confederation 2020

[17]. Carlos A. Felippa "Introduction to Finite Element Methods" Department of

Aerospace Engineering Sciences and Center for Aerospace Structures, University of Colorado, Boulder, Colorado 80309-0429, USA

[18]. J. N. Reddy, "Mechanics of Laminated Composite Plates and Shells: Theory and Analysis" (Applied and Computational Mechanics), CRC Press; 2nd edition (November 24, 2003)

[19]. Marco Esposito, Rinto Roy, Cecilia Surace and Marco Gherlone,"Hybrid Shell-Beam inverse Finite Element Method for the Shape Sensing of Stiffened Thin-Walled Structures: Formulation and Experimental Validation on a Composite Wing-Shaped Panel"

[20]. Adnan Kefal, Erkan Oterkus, Alexander Tessler, Jan L. Spangler, " A quadrilateral inverse-shell element with drilling degrees of freedom for shape sensing and structural health monitoring", 2016

[21]. A. Tessler, T.J. Hughes, "An improved treatment of transverse shear in the Mindlin-type four-node quadrilateral element", Comput. Methods Appl. Mech. Eng. 39 (3) (1983) 311–335.

[22]. Marco Esposito , Massimiliano Mattone, Marco Gherlone "Experimental Shape Sensing and Load Identification on a Stiffened Panel: A Comparative Study" 2022

[23]. Foss, G.; Haugse, E. "Using modal test results to develop strain to displacement transformations." In Proceedings of the 13th International Modal Analysis Conference, Nashville, TN, USA, 13–16 February 1995.

[24]. Pisoni, A.C.; Santolini, C.; Hauf, D.E.; Dubowsky, S. "Displacements in a vibrating body by strain gauge measurements." In Proceedings of the 13th International Modal Analysis Conference, Nashville, TN, USA, 13–16 February 1995.

[25]. Gherlone, M.; Cerracchio, P.; Mattone, M. "Shape sensing methods: Review and experimental comparison on a wing-shaped plate." Prog. Aerosp. Sci. 2018

[26]. Esposito, M.; Gherlone, M. "Composite wing box deformed-shape reconstruction based on measured strains: Optimization and comparison of existing approaches." Aerosp. Sci. Technol. 2020

[27]. Shkarayev, S.; Krashanitsa, R.; Tessler, A. "An inverse interpolation method utilizing in-flight strain measurements for determining loads and structural response of aerospace vehicles." In Proceedings of the 3rd International Workshop on Structural Health Monitoring, Stanford, CA, USA, 12–14 Septemember 2001.

[28]. Airoldi, A.; Marelli, L.; Bettini, P.; Sala, G.; Apicella, A. "Strain field reconstruction on composite spars based on the identification of equivalent load conditions." In Sensors and Smart Structures Technologies for Civil, Mechanical, and Aerospace Systems 2017; Lynch, J.P., Ed.; International Society for Optics and Photonics: Bellingham, WA, USA, 2017;

[29]. Esposito, M.; Gherlone, M.; Marzocca, P. "External loads identification and shape sensing on an aluminum wing box: An integrated approach." Aerosp. Sci. Technol. 2021

[30]. Tessler, A.; Spangler, J.; Mattone, M.; Gherlone, M.; Di Sciuva, M. "Real-time characterization of aerospace structures using onboard strain measurement technologies and inverse Finite Element Method." In Proceedings of the 8th International Workshop on Structural Health Monitoring,Stanford, CA,USA,12–14 September 2011.

[31]. Kefal, A.; Yildiz, M. "Modeling of Sensor Placement Strategy for Shape

Sensing and Structural Health Monitoring of a Wing-Shaped Sandwich Panel Using Inverse Finite Element Method." Sensors 2017

[32]. Rinto Roy, Alexander Tessler, Cecilia Surace, Marco Gherlone "Shape Sensing of Plate Structures Using the Inverse Finite Element Method: Investigation of Efficient Strain–Sensor Patterns" 2020

[33]. Bruno, R.; Toomarian, N.; Salama, M. "Shape estimation from incomplete measurements: A neural-net approach." Smart Materials and Structures 1994

[34]. A. Tessler, J. Spangler, M. Gherlone, M. Mattone, and M. Di Sciuva, "Deformed shape and stress reconstruction in plate and shell structures undergoing large displacements: application of inverse finite element method using fiber-Bragg grating strains" in Proceedings of 10th World Congress on Computational Mechanics, Sao Paulo, Brazil, 2012.

[35]. Alexander Tessler, Rinto Roy, Marco Gherlone, Marco Esposito, Cecilia Surace, "Shape Sensing of Plate and Shell Structures Undergoing Large Displacements Using the Inverse Finite Element Method" 2018

[36]. Marco Esposito, Marco Gherlone "Composite wing box deformed-shape reconstruction based on measured strains: Optimization and comparison of existing approaches" 2020

[37]. W.L. Ko, W.L. Richards, V.T. Fleischer, "Applications of the Ko displacement theory to the deformed shape predictions of the doubly-tapered Ikhana wing", NASA/TP-2009-214652, 2009.

[38]. C. Pak, "Wing shape sensing from measured strain", AIAA J. 54 (3) (2016)

[39]. J. O'Callahan, P. Avitabile, R. Riemer, "System equivalent reduction expansion process" in: Proceedings of the 7th International Modal Analysis Conference, 1989, Las Vegas, 1988.